Aeronautical Research Institute, University of Tokyo
Report No. 334, August 1958

On the Fracture of Metals

By

Masuji UEMURA

Summary. The present paper is divided into three parts.

First of all, a phenomenological fracture hypothesis or criterion of polycrystalline metals was presented in a general form in Part I. A method to predict the fracture stresses under polyaxial uniform stresses was shown and the experimental fracture results of ductile metals were well explained. Moreover, qualitative views on the problem of low temperature brittle fracture and the effects of prestrains were also shown from a consideration of temperature characteristics of fracture stress surface.

Next, in Part II, the author attached importance to the fact that the difficulties of analysing the stress and strain distributions at the moment of fracture cause much complexity in practical fracture problems, and carried out tensile fracture tests of mild steel round bars having hyperbolic notches. After analysing their distributions across the minimum section, the author explained the fracture stresses together with various fracture behaviors by using the fracture criterion and presented a qualitative view as to the notch brittleness phenomenon.

Lastly, to ascertain the validity and applicability of this criterion to brittle metals, the author carried out fracture tests on thin-walled gray cast iron tubes under various ratios of combined tension and torsion in Part III. First, the peculiarities arising in elastic and plastic deformations under combined stresses and absent in ductile metals were discussed with due account of the notch effect due to the heterogeneous graphites in pearlite matrix. Secondly, the fracture behaviors under combined stresses were discussed by taking into account the mechanism of deformation and applying the fracture criterion at the tip of graphite flake. Furthermore, the findings of other research students under other kinds of polyaxial stresses are cited and discussed for purposes of analysing the criteria proposed by others.

From all the descriptions, the reasonableness of the author's fracture criterion on polycrystalline metals seemed to be established.

PART I. FRACTURE CRITERION

1.1. INTRODUCTION

The fact that the nature of fracture has been, as yet, very little understood with the exception of Griffith's theory developed for glass etc., results from the incomplete knowledge regarding the effects of various influence variables. These can be resolved into two parts: One is concerned with the metallurgical variables and the microscopic mechanisms of fracture, and the other with the effects of testing

variables, which might be called "external variables" on fracture. In the present paper, problems concerning the latter will be discussed in the fracture criterion of metals.

The fracture criterion of metals is of very great significance not only for brittle materials, but also for ductile materials for interpreting the problems of notch brittleness and plastic working etc. It seems to the author that the various kinds of laws for fracture suggested so far are not presented in a general form so as to be applicable commonly to many kinds of materials under general polyaxial stress states. In view of the above situation, the author has presented here, first of all, a phenomenological fracture hypothesis or criterion of polycrystalline metals in a general form. The two effects, that is, of stress polyaxiality and of plastic deformation on fracture, which are particularly dominant in various factors influencing fracture, were formulated mathematically in this fracture criterion. Here were assumed the existence of the fracture stress surface such as introduced by Ludwik [*1*] and the existence of two inherent modes of fracture: ductile shear fracture and brittle tensile fracture, in engineering metals. The author intends to apply this criterion without distinction of the so-called ductile or brittle materials defined by the intuitive fracture behaviors and to predict the fracture stresses under arbitrary states of combined stress. These two major factors especially considered here have been already indicated in previous works and experiments. Such an attempt at mathematical formulation has been also seen in the excellent study by Profs. Yoshiki and Kanazawa [*2*], in which the problem of notch brittleness seemed to be the main object of their research.

In addition to the presentation of the fracture criterion, the experimental results of fracture of ductile metals under combined stress have been explained on the basis of this criterion in this paper, and qualitative views on the problem of brittle fracture at low temperature and the effects of prestrains are also shown from a consideration of temperature characteristics of fracture stress surface.

1.2. Presentation of Fracture Criterion

Hitherto, the materials have been intuitively classified by the fracture behaviors under simple stress state at room temperature as brittle material or ductile material, and the kind of stress to prescribe the fracture in the criterion has been designated according to the kind of material in most cases. However, such a distinction between these two kinds of materials is considered to be convenient and to depend on the circumstances of stress loading. In addition, the fracture mechanism of metals can be classified into a number of types according to the metallurgical or physical factors, as pointed out by Orowan [*3*]. In such complex circumstances of fracture, the present author selected especially the two main types of fracture, that is, the brittle (cleavage) fracture and the ductile (shear) fracture, under statical loading at (or below) room temperature, excluding creep fracture under high temperature, fatigue fracture under alternating stress, and other special types of fracture.

(1) *Two Types of Fracture*

It is usual that in the shear type of fracture, considerable plastic deformation precedes the fracture, while in the cleavage type of fracture, there is little plastic deformation. The former phenomenon can be usually seen in ductile materials which are apt to undergo plastic deformation accompanying stress relaxation, while the latter can be seen in brittle materials, which are not apt to deform plastically with stress concentration. The meanings of these two modes of fracture will be simply discussed as follows with consideration of the fracture mechanism.

First, the cleavage (tensile brittle) fracture is considered to be due to a mechanism similar to the Griffith type fracture. However, it appears probable that the Griffith cracks in metals as a cause of local stress concentration are of a different nature from that of truly brittle materials such as glass or ceramics. Even in brittle metals, small plastic deformation ahead of the tips of cracks have been recognized. According to the microscopic consideration in the dislocation theory, the concentrated tensile stress is assumed to be produced by the arrays of blocked dislocations leading to the cleavage fracture, so the slip planes in which dislocations are held up at grain boundary can be identified with the Griffith cracks (Zener [*4*]). In addition, nonmetallic inclusions or secondary metallurgical phases etc. may be considered as causes of stress concentration in metals (Hollomon [*5*]). From an engineering sense, it will be convenient to difine the cleavage fracture of metals in a broader sense by including them as sources of Griffith cracks. All cleavage fracture are not brittle fractures, since it is possible to see a cleavage fracture, for instance, under such testing conditions as under high rate of straining, triaxial stress, low temperature, or stress concentration due to notch etc. in which it is difficult for further plastic deformations to occur.

Secondly, the shear (slip, ductile) fracture is considered to be a process of slipping apart by the linking together of a number of micro-cracks due to plastic deformations such as slips, twinnings, or kinkings etc. in crystal grains. The shear is an essential part of ductile fracture and considerable plastic deformations usually precede the fracture.

The two modes of fracture considered in the criterion correspond to the distinguishable fracture behaviors in that the macroscopic fracture surfaces are almost nearly normal to maximum tensile stress (σ_m) or along maximum shearing stress (τ_m) as observed in the various experiments. Regardless of the similar micromechanism in the two types of fracture in polycrystalline metals, such a noticeable discontinuous variation in directions of fracture surfaces is exhibited according to the differences of testing conditions. This problem is left to be interpreted as a subject of further study in the future.

(2) *Fracture Conditions and Fracture Stress Surfaces*

Ludwik [*1*] introduced a conception of fracture, in which the fracture point is the intersection of a fracture stress curve with a flow stress curve (stress-strain curve) in simple one-dimensional consideration. The author's conception is based on a similar hypothesis as Ludwik's, in which the conditions for plastic flow and

for fracture are independent of each other. As above indicated, the metals exhibit in common two modes of fracture inherently at or below room temperature. By taking this into account, the author considered two kinds of limiting fracture stresses: limiting shear stress τ_{cr} and limiting tensile stress σ_{cr}, as Davidenkov [6] did, modifying Ludwik's conception.

Then, the fracture conditions will be defined as follows. When the maximum shear stress τ_m or the maximum tensile stress σ_m during plastic flow (evaluated by using the law of plastic flow described in (3)) reaches the limiting shear stress τ_{cr} or the limiting tensile stress σ_{cr} on fracture (as will be described later in detail in this paragraph), respectively, then the fracture takes place in either type, depending on which intersection is achieved earlier. As a result, the fracture condition will be given in either of the following equations.

$$\tau_m \geq \tau_{cr} \quad \text{or} \quad \sigma_m \geq \sigma_{cr} . \tag{1}$$

Next, we restrict our consideration to the fracture stress. The two fracture stress curves in Davidenkov's hypothesis are expressed in one-dimensional form and the curve for ductile fracture has a negative slope with increasing plastic strain, being different from the author's as will be shown later.

Both types of fractures of metals are always accompanied by plastic deformations which produce work hardening or cold working. In addition, as Mott [7], Zener [8], Yokobori [9], and others suggested, using the concept of dislocation, the fracture mechanism is related to tensile stress, not to mention shear stress. For example,

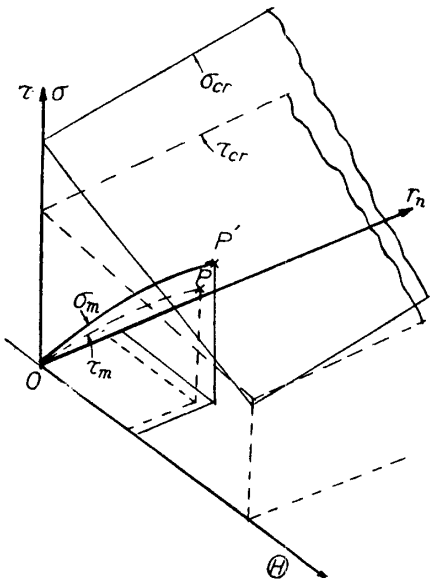

FIGURE 1. Fracture stress surface and flow curve.

if the Griffith cracks are arrays of blocked dislocations, the concentrated tensile stresses are then controlled by the shear stress acting on the dislocations. The above two factors are designated as the effects of the entire strain histories preceding fracture and of the stress state at fracture, respectively. These two major factors were formulated mathematically in the expression of the critical fracture stress in this fracture criterion, the remaining influence factors, such as strain rate,

stress gradient, size effect etc. being neglected as second-order correction effects.

From the above viewpoint, both limiting fracture stresses τ_{cr} and σ_{cr} are assumed to depend on the entire plastic prestrain up to fracture and the triaxiality of stress at fracture and to be expressed approximately as flat surfaces in the linear functional dependence on γ_n (octahedral shear strain) and Θ (mean stress or hydrostatic tension). The fracture stress surfaces are shown in Fig. 1 in three-dimensional chart and expressed mathematically as

$$\tau_{cr}=a+b\Theta+c\gamma_n, \tag{2a}$$

$$\sigma_{cr}=a'+b'\Theta+c'\gamma_n, \tag{2b}$$

where $a,\cdots; a',\cdots$ are the material constants which are fuctions of temperature, strain rate and metallurgical factors etc. γ_n and Θ are shown by

$$\left.\begin{aligned}\gamma_n&=(2/3)\cdot\{(\varepsilon_1-\varepsilon_2)^2+(\varepsilon_2-\varepsilon_3)^2+(\varepsilon_3-\varepsilon_1)^2\}^{\frac{1}{2}},\\ \Theta&=(\sigma_1+\sigma_2+\sigma_3)/3\end{aligned}\right\} \tag{3}$$

respectively.

The ambiguous term "triaxiality" cited in the problems of notch brittleness is here analytically expressed with the use of the terms of γ_n and Θ, because the criterion should be expressed logically in a function of three-dimensional invariants on stress and strain.

First of all, the fracture stresses increase linearly with increasing γ_n. As already indicated by various experiments [*10*] concerning the effects of plastic deformations on fracture, the resistance to fracture is increased by the strain hardening. Contrary to this positive slope against plastic strain, Davidenkov [*6*] introduced a negative slope. The author supposes that this was introduced to explain the decrease of fracture stress with increasing strain preceding fracture in the ductile fracture, which can be seen in the curve named "Technical cohesive strength curve" by Kuntze [*11*] in the experiments with notched specimens. (This experimental evidence will be explained later by the author's fracture criterion in Part II). In this criterion, let the slopes of both fracture stress surfaces be positive with respect to γ_n. γ_n, as a representing factor of the effect of prestrain on fracture, has been used also in the work by Profs. Yoshiki and Kanazawa [*2*].

Secondly, the fracture stresses decrease linearly with increasing Θ. While the plastic flow curve is independent of Θ, the dependence of fracture stress on the triaxiality of stress has been well demonstrated in experiments by Bridgman [*12*] and others [*13*] [*14*].

The rates of decrease against Θ and of increase against γ_n are thought to be larger in the σ_{cr} surface than in the τ_{cr} surface, according to the experimental evidences indicating that metals are apt to fracture in cleavage accompanying smaller strains under high triaxial tensile stress states and to fracture in shear accompanying larger plastic strains under simple uniaxial or low triaxial tensile stress states.

(3) *Law of Plastic Flow*

The plastic flow curve necessary for determining the intersection with the frac-

ture stress surface may be discussed with basis on the octahedral shear stress theory according to the plastic deformation theory, excepting in the cases of complicated loading proceses. It has been shown that the stress-strain relations of ductile isotropic metals under various combined stress states are uniquely described with few errors and are determined by simple uniaxial tensile tests. This law of plastic flow cannot be applied as it stands to brittle materials such as gray cast irons which are far from being isotropic or homogeneous and there is need of some corrections by taking into account the notch effects of inclusions such as graphite carbons, as will be discussed later in Part III.

In the case of ductile materials, the law of plastic flow can be expressed as follows, with the introduction of the coeffient of plasticity D,

$$\left.\begin{aligned} &\varepsilon_1=[\sigma_1-(\sigma_2+\sigma_3)/2]/D\,,\\ &\varepsilon_2=[\sigma_2-(\sigma_3+\sigma_1)/2]/D\,,\\ &\varepsilon_3=[\sigma_3-(\sigma_1+\sigma_2)/2]/D\,,\\ &\text{where}\quad D=f(\gamma_n)\quad\text{or}\quad g(\tau_n)=3\tau_n/\gamma_n\,,\\ &\tau_n=(1/3)\cdot\{(\sigma_1-\sigma_2)^2+(\sigma_2-\sigma_3)^2+(\sigma_3-\sigma_1)^2\}^{\frac{1}{2}}\,. \end{aligned}\right\} \qquad (4)$$

After an analysis of the stress and strain distributions by the use of the above law of plastic flow, the flow curves of τ_m and σ_m are represented schematically in Fig. 1 as OP and OP′ curves, respectively. The location and the mode of inital fracturing will be determined by the intersection of the fracture stress surfaces and the corresponding flow curves, which will occur first.

As a summary, if we take into consideration both mechanisms of fracture and define σ_{cr} and τ_{cr}, not as constant values, but in a general functional form as done in this criterion, each of the previously proposed criteria can be included as a special one of this criterion. And we can settle the disagreements with experimental results pointed out when these criteria such as the maximum tensile stress theory or the maximum shearing stress theory, etc., are used. Moreover, the mathematical derivations for fracture stresses become easier as will be indicated in the next chaper.

Finally, a suplement on the directions of microscopic fracture surfaces is added. They are not always consistent with the directions of σ_m or τ_m, for the mechanism of fracture is not governed by σ_m or τ_m as already explained from the concepts of dislocations, and the meaning of this fracture is that the fracture is merely determined according to whether or not σ_m or τ_m is equal to σ_{cr} or τ_{cr} given in a form of functional dependence of γ_n and θ. These correspond to the analogous argument that in the Mohr's theory in plane stress, there is not necessarily real contact between the stress circle for fracture and the envelope, therefore the criterion should be given in the functional dependence of τ_m on the mean stress, which is to be determined by experiments and, further, the failure would take place in the direction corresponding to the real contact point between them [*15*]. These arguments were ascertained in the relation between the yield criterion and the direction of slip bands observed in the yield of mild steels in experiments carried out by the author [*16*].

1.3. Application of Fracture Criterion—Method of Determining Limiting Fracture Stress Surfaces and Fracture Stresses in Ductile Metals, and Comparisons with Experimental Results

If the effects of Θ and γ_n in Eqs. (2) are neglected as small quantities, then the criterion reduces naturally to maximum shear stress law or maximum tensile stress law. The ductile materials such as brass (see Fig. 2), Mg alloys (see Fig. 3), Al alloys etc. fracture in shear in all fields of biaxial stresses; however, the brittle materials such as cast irons exhibit two types of fracture, which will be discussed in detail later in Part III. In this chapter, as an example of application of this criterion, the ductile isotropic materials exhibiting shear fracture will be first considered.

Taking into account the experimental evidences indicating that the values of τ_n at fracture are not much different in ductile materials and the flow curve (τ_n versus γ_n curve) can be approximated by a linear line near the fracture point, the flow curve can be written as

$$\gamma_n=\alpha\tau_n+\beta\,, \tag{5}$$

then Eq. (2.a) reduces to

$$\tau_{cr}=(a+c\beta)+b\Theta+c\alpha\tau_n\,. \tag{6}$$

Three coeficients; $(a+c\beta)$, b and $c\alpha$ in the right hand side of Eq. (6) can be expressed in terms of three experimental fracture stresses f_t, $-f_c$ and f_s under simple tension, compression and torsion, respectively, after τ_{cr}, Θ and τ_n have been expressed by these fundamental material strengths and the three algebraic equations of first order have been solved. Experiments under combined stresses are usually carried out in thin cylinders under axial load and internal pressure which produces a nearly biaxial field of stress. In such a fracture experiment, whose results are shown in Fig. 3, the ratio of the radial stress σ_3 to the tangential stress σ_2 can be taken as constant $(-k)$.

$$\sigma_3/\sigma_2=-k\,. \tag{7}$$

Then τ_{cr} in Eq. (6) can be finally expressed as

$$\begin{aligned}\tau_{cr}=[&2(2-\sqrt{3})\xi\eta f_t+(2-\sqrt{3})(1-\xi)\eta\sigma_1(1+\mu-k\mu)+2\{\xi-\eta(1+\xi)\}|\sigma_1|\times\\ &\sqrt{\mu^2(1+k+k^2)-\mu(1-k)+1}\,]/2\{2\xi-\sqrt{3}\,\eta(1+\xi)\}\end{aligned} \tag{8}$$

where $\xi=f_c/f_t$, $\eta=f_s/f_t$, $\mu=\sigma_2/\sigma_1$, $\sigma_1=$the axial stress.

The shear fracture stresses under arbitrary combined stress states will be calculated from the following conditions by taking into account the different directions of maximum shear stress in each field of stress (A), (B) and (C) in Fig. 3, and taking τ_{cr} equal to τ_m.

$$\left.\begin{aligned}\tau_{cr}&=(\sigma_1-\sigma_3)/2=\sigma_1(1+k\mu)/2 \cdots \text{field} \quad \text{(A)},\quad 0\leqq\mu\leqq 1\\ &=(\sigma_2-\sigma_3)/2=\sigma_1\mu(1+k)/2 \cdots \;,, \quad \text{(B)},\quad -k\leqq 1/\mu\leqq 1\\ &=(\sigma_2-\sigma_1)/2=\sigma_1(\mu-1)/2 \cdots \;,, \quad \text{(C)},\quad -1/k\leqq\mu\leqq 0\end{aligned}\right\} \tag{9}$$

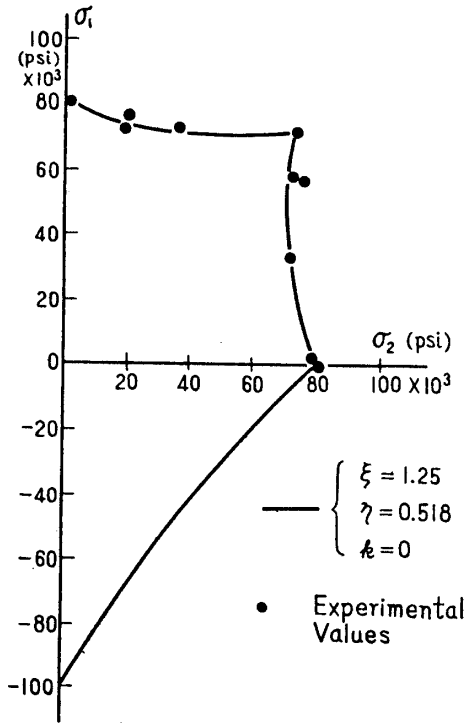

FIGURE 2. Fracture stresses on brass under biaxial combined stresses (McAdam) and analytical results.

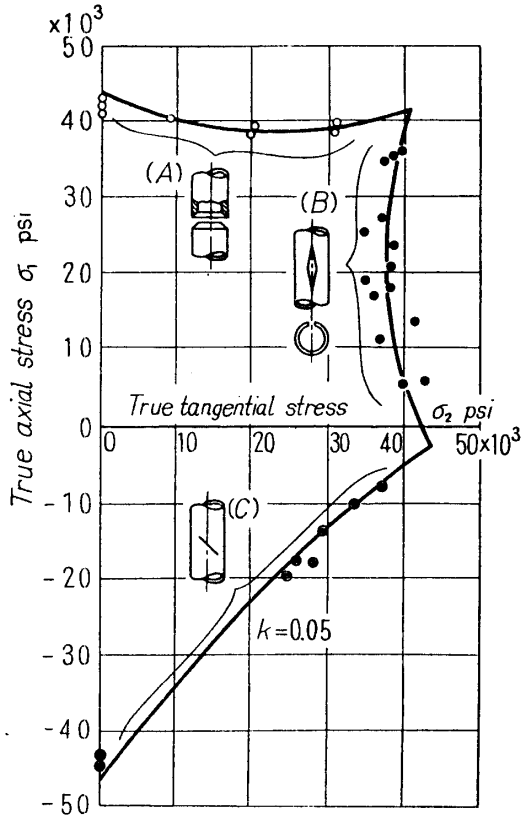

FIGURE 3. Fracture stresses on FS$_{-1}$ Mg alloy tubular specimens under biaxial combined stresses (E. G. Thomsen & J. E. Dorn) and analytical results.

By equating Eqs. (9) to Eq. (8), the fracture stresses in each field under combined stress states can be predicted by the following equations.

$$\left.\begin{aligned}
\frac{\sigma_1}{f_t} &= \frac{2(2-\sqrt{3})\xi\eta}{2\{\xi-(1-\xi+\sqrt{3}\,\xi)\eta\}+\mu[2k\{\xi-(\sqrt{3}-1+\xi)\eta\}+(2-\sqrt{3})(\xi-1)\eta]} \\
&\quad \overline{-2\{\xi-\eta(1+\xi)\}\sqrt{\mu^2(1+k+k^2)-(1-k)\mu+1}}, \cdots \text{in the field} \quad \text{(A)} \\
\frac{\sigma_2}{f_t} &= \frac{2(2-\sqrt{3})\xi\eta}{2\{\xi-(1-\xi+\sqrt{3}\,\xi)\eta\}+2k\{\xi-(\sqrt{3}-1+\xi)\eta\}+(2-\sqrt{3})(\xi-1)\nu\eta} \\
&\quad \overline{-2\{\xi-\eta(1+\xi)\}\sqrt{(1+k+k^2)-(1-k)\nu+\nu^2}}, \cdots \text{in the field} \quad \text{(B)} \\
\frac{\sigma_2}{f_t} &= \frac{2(2-\sqrt{3})\xi\eta\mu}{\mu[2\{\xi-(1-\xi+\sqrt{3}\,\xi)\eta\}-k\eta(2-\sqrt{3})(\xi-1)]-2\{\xi-(\sqrt{3}-1+\xi)\eta\}} \\
&\quad \overline{+2\{\xi-\eta(1+\xi)\}\sqrt{\mu^2(1+k+k^2)-(1-k)\mu+1}}, \cdots \text{in the field} \quad \text{(C)}
\end{aligned}\right\} \tag{10}$$

where $\nu=\sigma_1/\sigma_2=1/\mu$.

As an actual example, the results of experiments with brass [*14*] are shown in Fig. 2. We can put k nearly equal to zero in the case of very thin cylinders. Strictly speaking, it will be necessary to analyse the stress distributions along the thickness to determine what value of k should be taken. These experimental

results shown in Fig. 2 agree fairly well with the solid line obtained theoretically by using Eq. (10) if $k=0$, $\xi=1.25$, $\eta=0.518$.

Similar experimental results with FS_{-1} Mg alloys [*17*] are shown in Fig. 3, where the agreements between experimental results and theoretical calculations shown by a solid line are also very good. This solid line is obtained by putting $k=0.05$, $\xi=1.2$, $\eta=0.5$.

In the analytical derivation of Eq. (10), the flow curve near the fracture point was assumed to be linear, however, in the cases of materials having curved stress-strain relation, the fracture stresses can be obtained graphically. That is, both curves of τ_{cr} and τ_m can be plotted in the same $\tau\sim\Theta$ diagram by taking γ_n (or τ_n) as a parameter, then the shear fracture stress can be obtained from the intersection point of these two corresponding curves of the same value of γ_n (or τ_n).

As shown above, the experimental results can be well explained, and these agreements have been seen also in Al alloys [*14*] and mild steels [*18*]. It seems that the experimental results will be explained better, if the effects of anisotropy neglected here are taken into consideration.

The fracture stresses for $\mu=0$, 1 and ∞ are comparatively high, presenting cusps in the fracture stress curves in Figs. 2 and 3, which can be attributed to the effects of plastic strains or strain hardening; and the fracture stress for $\mu=1$ is lower than that for $\mu=0$ and ∞, which can be attributed to the effects of hydrostatic tension Θ.

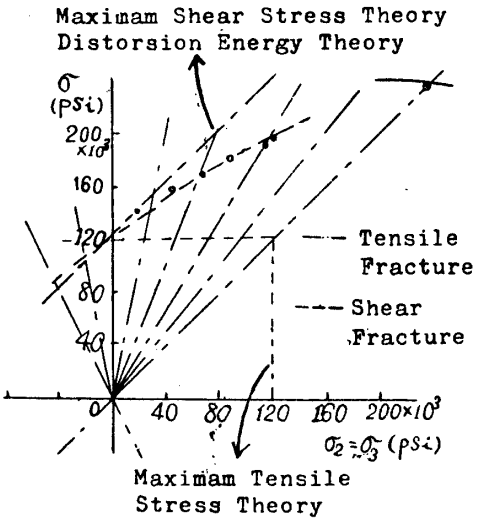

FIGURE 4. Fracture stresses on 0.61% carbon steel under triaxial combined stresses.

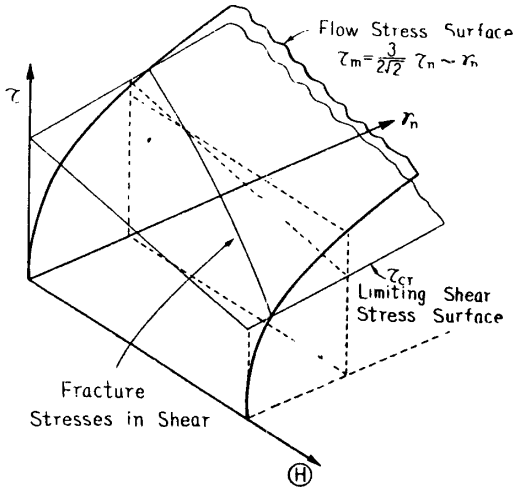

FIGURE 5. Diagram for obtaining fracture stresses under triaxial stresses, of which two principal stresses are equal.

As an example of purely triaxial stress states, the experimental fracture results for 0.61% carbon steel [*14*] in a special case of $\sigma_2=\sigma_3$ are shown in Fig. 4. It seemed that the fractures took place in shear fracture in the range of $\mu=0\sim0.6$ and the fracture under pure hydrostatic tension took place in tensile fracture at $\mu=1$, therefore, the former is considered here. The fracture stresses can be also obtained analytically or graphically in a manner similar to that above. However,

the trends of shear fracture can be easily understood from the following considerations.

In this special loading condition ($\sigma_2=\sigma_3$), there exists a following relation between τ_m and τ_n.

$$\tau_m=3\tau_n/2\sqrt{2}=(\sigma_2-\sigma_1)/2\,. \tag{11}$$

The flow law ($\tau_n\sim\gamma_n$) being independent of Θ, the flow curve of τ_m can be expressed by a curved surface parallel to the axis of Θ as shown in Fig. 5. Adding the shear fracture stress (τ_{cr}) surface also in the same figure, the fracture stresses can be graphically defined as the intersecting line of both surfaces. The fracture strains decrease with increasing Θ showing embrittleness and the decrease of shear fracture stresses ($=\tau_{mr}=(\sigma_{1r}-\sigma_{2r})/2$, suffix "$r$" denotes the value at fracture) can be well explained in agreement with the experimental results in Fig. 4. It is clear that these results cannot be explained by other proposed criteria for fracture as shown in Fig. 4. Even though the differences between this criterion and other proposed criteria are not quantitatively distinguishable in biaxial stress states, the differences in triaxial stress states become distinguishable showing greater decrease of shear fracture stress and ductility than in biaxial cases. Therefore, the significance of these fracture problems under polyaxial stress states is to be appreciated in connection with the tests on notched (or necked) tensile specimens as will be shown later in Part II. The fracture stresses in hydrostatic compression will become extremely higher, and the experimental indication that the fracture does not take place in pure hydrostatic compression also can be easily understood from the above discussion.

1.4. A View as to the Low Temperature Characteristics of Limiting Fracture Stress Surface

Steels which show the ductile fracture at room temperature show cleavage brittle fracture at low temperature. A quantitative treatment of the effects of temperature was excluded from this criterion by including them in the material constants in Eq. (2). A view concerning the brittle fracture phenomenon at low temperature will be qualitatively discussed here by considering the low temperature characteristics of limiting fracture stress surfaces.

The yield stress increases and the elongation decreases with lowering temperature in tensile tests of steels, while the fracture stress also increases, but much less than does the yield stress. J. H. Hollomon [*19*] suggested the dependencies of yield and fracture stresses on temperature under constant strain rate by the following formulas,

$$\left.\begin{aligned}\sigma_Y\ (\text{yield stress})&=Ae^{S/T}\,,\\ \sigma_B\ (\text{fracture stress})&=Be^{U/T}\,,\end{aligned}\right\} \tag{12}$$

where T=absolute temperature, A, B=material constants in function of strain rates, S, U=material constants ($S>U$).

The rise of the fracture stress at low temperature can be due to the major reason that occurrence of plastic deformations becomes difficult, as a result of which micro-cracks as sources of fracture are not produced.

The flow stress-strain curves become steeper under low temperature, whereby the reduction of fracture strain can be easily understood. Even though the low temperature characteristics under simple tensile tests can be expressed in practice as in Eq. (12), it is doubtful whether or not the dependencies of fracture stress surface on temperature under combined stress can be simply expressed in a form of $e^{\text{const}/T}$ independently of γ_n and θ. It seems convenient to consider their dependencies on τ_{cr} and σ_{cr} surfaces due to different fracture mechanisms separately.

To the author's regret, he has no experimental data under polyaxial stresses over a wide range of temperature; as a result, he is forced to be contented with qualitative conjecture because of the difficulties of quantitative treatments. The rise of fracture stress surface with lowering temperature seems to be smaller in the field of large θ and small γ_n compared with other fields. This tendency is considered to be remarkable in the σ_{cr} surface, because the cleavage fracture is caused chiefly by the notch effect due to cracks and the propagation velocity of cracks is so fast that the phenomenon cannot be discussed as a rate process and, consequently, the fracture is independent of thermal activation and is not greatly influenced by temperature.

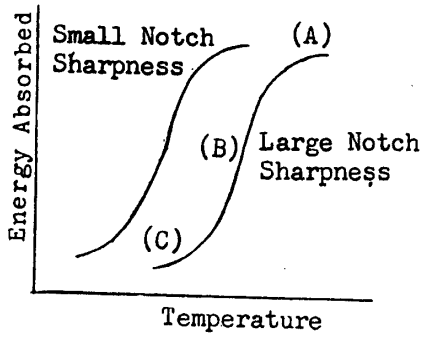

FIGURE 6. Notch brittleness phenomenon.

The typical trends of temperature dependency of energy absorbed in impact tests are shown in Fig. 6 in reference to notch brittleness. A rapid drop of energy absorption in the narrow interval of temperature referred to as "transition temperature" may be explained as follows: It is due to the existence of discontinuity in the gradients of both fracture stress surfaces accompanied by the change of fracture mechanism on greater parts of fractured surface of specimen from shear to cleavage fracture. With sharp notches, γ_n is small under high hydrostatic tension θ not exhibiting plastic deformation, and the σ_{cr} surface is especially low at low temperature, so the fractures are chiefly caused by cleavage fracture in the range denoted (C) below transition temperature, while in the range denoted (A) above transition temperature accompanying plastic deformation is due to the low τ_{cr} surface under higher temperature. In the intermediate range called transition temperature, both modes of fracture coexist in the same order. This consideration

may be admitted as reasonable from the fact that the relation between the depth of shear fractured part in the notched specimen and temperature shows a closely similar trend to that as shown in Fig. 6.

In the previous research work on notch brittleness, most of the information available is in terms of transition temperature in notch impact tests from the practical point of view, and the relations with width or thickness of plate or notch sharpness in addition to metallurgical factors have been discussed as the object of study. Nevertheless, the main factor in this phenomenon is considered to be the triaxiality of stress besides the rapid strain rate under impact loading; so a study of analysing the stress and strain distributions in addition to the temperature dependency of limiting fracture stress surface becomes necessary. The former part of the problem will be considered in Part II.

1.5. The Explanation of Experiments on the Effects of Prestrains

Now let us restrict the problem to the case of unnotched specimens under simple uniaxial tension. The fracture stresses of the specimens prestrained are the same as those of unprestrained specimens under the same loading condition and at the same temperature [*20*]. As an example of these experimental evidences, the results on polycrystal copper [*21*] subjected to various degrees of prestrains are shown in Fig. 7. In this case, the total strains up to fracture after initial loadings are almost the same regardless of the amounts of prestrain. As a result, the effects of prestrains can be included in the criterion by taking the total plastic strain as γ_n, excepting in the case of complicated loading processes.

The following experiments have been carried out to see the effects of prestrains; that is, after being subjected to various degrees of tensile prestrains at room temperature, the specimens have been subsequently pulled to fracture in tension under

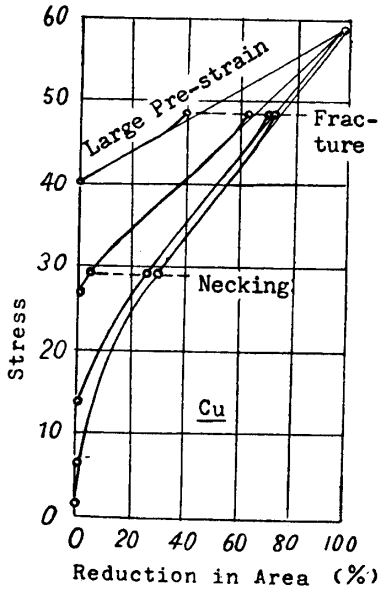

FIGURE 7. Effect of prestrain on the fracture stress on copper in simple tension ([*21*]).

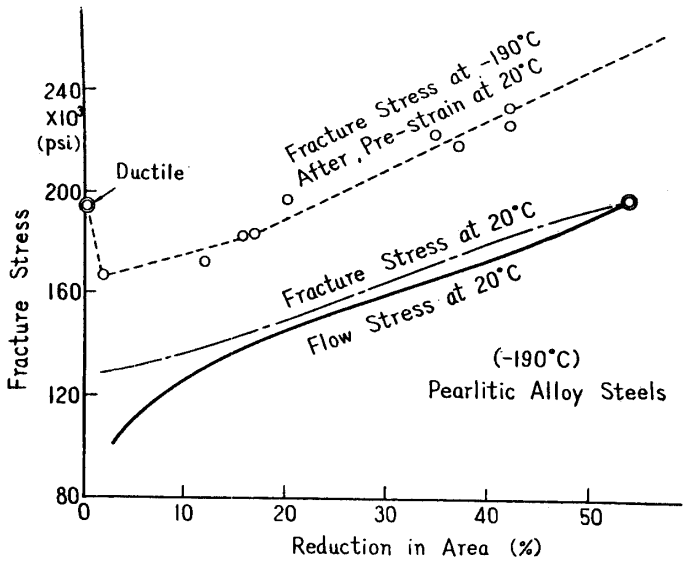

FIGURE 8. Effect of prestrain at room temperature on the fracture stress in subsequent testing at low temperature (Hollomon and Zener).

extremely low temperature sufficient to prevent further additive plastic strains [*19*] [*20*]. As an example of this experimental process, the tensile fracture test results on pearlitic alloy steels [*22*] under extremely low temperature (−190°C) after they were subjected to tensile prestrain at room temperature (20°C), are shown in Fig. 8. The intersection point of the flow curve at room temperature and the hypothetical fracture stress curve at the same temperature indicates the fracture at the room temperature which is shown as the value on the ordinate at zero prestrain. Higher values of the fracture stresses under low temperature at the higher prestrains were obtained, and the fracture stresses after small prestrains are rather lower than those at room temperature. It is likely that such well-known experimental results are due not only to effects of prestrains, but also mainly to the temperature characteristics of fracture stress surface discussed in Section 1.4. Since the fracture is caused by brittle tensile fracture at low temperature, these results can be accounted for by taking into account the temperature characteristics of the σ_{cr} surface as shown schematically in Fig. 9.

When the specimens are prestrained at room temperature, the flow curve is on the flow surface at room temperature through the course of $\overrightarrow{OP}$. P denotes the

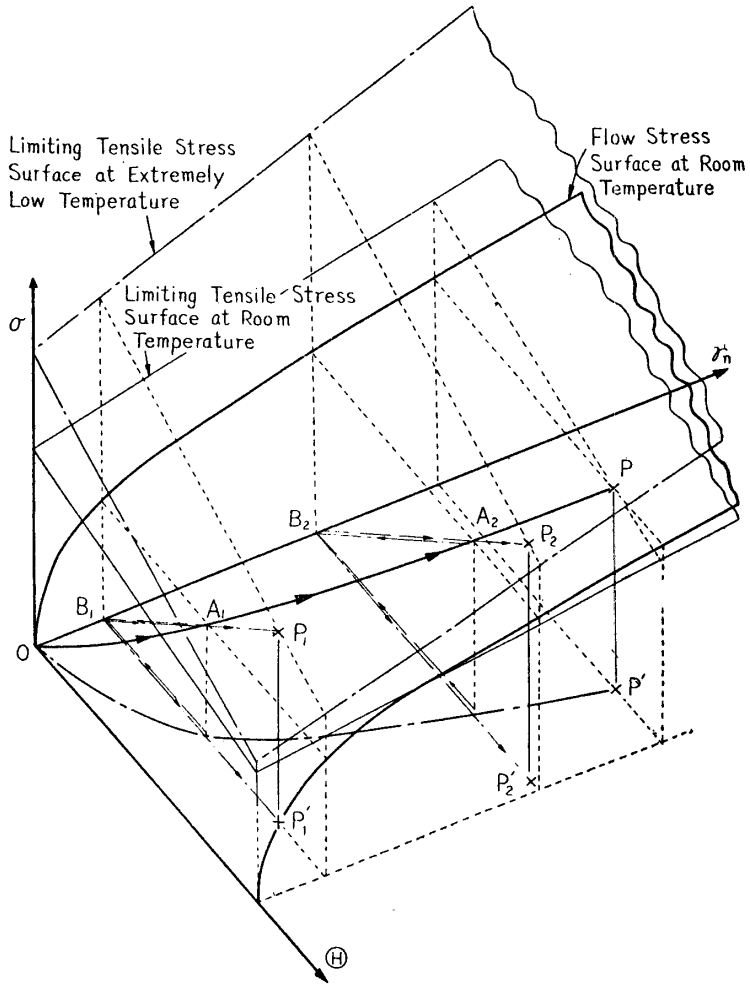

FIGURE 9. Diagram for explaining fracture stresses at low temperature.

fracture point which is the point of intersection with the fracture surface; then PP′ denotes the value of fracture stress at room temperature. If the specimen is unloaded after being prestrained up to the A_i point, it remains at B_i, exhibiting permanent strain ($=OB_i$). The flow curve under reloading at low temperature takes a straight course $B_iA_iP_i$, where no new plastic strains are exhibited and then intersects at P_i with the fracture stress surface under low temperature, presenting an entirely brittle tensile fracture behavior. Then P_iP_i' denotes the fracture stress at low temperature. P_2P_2' in the case of larger prestrain is larger than PP′, because the surface at extremely low temperature is higher in the range of larger γ_n. On the other hand, P_1P_1' in the case of smaller prestrain is smaller than PP′, because the flow curve intersects with the σ_{cr} surface at extremely low temperature in the range of smaller γ_n, even though the σ_{cr} surface increases with decreasing temperature.

Although the fracture at room temperature is accompanied by shear ductile fracture in the outer part of fractured cross-section, the above discussion was based only on the consideration of the σ_{cr} surface. This is because of the consideration of the fact that the fracture commences in tensile fracture at the central axis (to be shown in Part II). And, as the distribution of σ_m in the axial direction along the necked cross section is not uniform, let PP′ denote the mean stress.

The above explanation is certainly not so much quantitative as qualitative; however, it seems that the experimental results on prestrains are well interpreted with this criterion and the supposed temperature characteristics of fracture stress surface.

Part II. Tensile Fracture Tests of Mild Steel Round Bars Having Hyperbolic Notches and Notch Brittleness

2.1. Introduction

It has been well known that notched specimens of ductile metals show brittle fracture because of the resulting polyaxial stress state, especially under low temperature. In view of these experimental evidences, the fractures in all-welded ships or aeroplanes flying at high altitude have been the subject of much attention in recent years in practical engineering fields. The problems of notch brittleness have been hitherto discussed chiefly from the viewpoint of practical necessity, the transition temperature in impact tests being stressed as the subject for research, and the fundamental problem remains unexplained quantitatively. The difficulty of analysis results from unknown stress and strain distributions at fracture in addition to the ambiguous fracture criteria and many parameters involved in this phenomenon. To the author's regret, the stress and strain distributions in notched tensile specimens of metals with strain hardening have not been analysed so far.

With this background, the author attached weight to the analysis of stress and strain distributions in this study and carried out tensile fracture tests of mild steel round bars having hyperbolic notches so that the analysis might be relatively easy.

After measuring minutely the average axial stress and strain across the minimum section at the moment of fracture with electric resistance wire strain gauge devices, the author analysed both distributions approximately and explained the fracture stresses together with various fracture behaviors by applying the fracture criterion to them and presented a qualitative view as to the notch brittleness phenomenon.

2.2. Test Procedure

(1) *Test Specimens*

The dimensions and the shapes of cylindrical tensile specimens having circumferential hyperbolic notches (Neuber type) are shown in Fig. 10 (a). The radius of curvature at the notch bottom has different degrees of size shown in Table 1, the minimum section being kept as constant. a_0 and b_0 denote the lengths of major and minor axes of the hyperbola, respectively. Further, unnotched tensile cylindrical specimens of uniform cross section ($2a_0=12$ mmϕ) such as shown in Fig. 10 (b) were used for conventional tensile tests to obtain the inherent static strengths of this material.

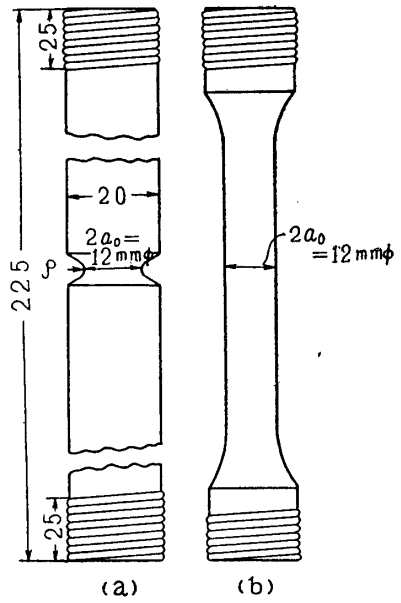

Figure 10. Tensile test specimens.

Table 1. Radius of curvature at the notch bottom and variation of notch sharpness due to tensile loading

Type	Initial radius of curvature ρ_0 (mm)	Notch sharpness	
		initial $\lambda_0=a_0/\rho_0$	at moment of fracture $\lambda=a/\rho$
(0)	∞	0	0.84
(i)	6.000	1	1.40
(ii)	1.500	4	1.75
(iii)	0.667	9	2.25
(iv)	0.375	16	2.80

Several specimens were tested for each one of the above five kinds of specimens. These specimens were taken from commercial low carbon steel bars (22 mmϕ), and, after machining, they were annealed in a furnace at about 870°C for one hour, then cooled in a furnace to eliminate the effects of machining. The chemical composition of mild steel used for this test was as follows:

C 0.18%, Si 0.11%, Mn 0.43%, P 0.036%, S 0.55%, Cu 0.28%.

(2) *Test Machine and Test Procedure*

The scheme of the entire experimental arrangement is shown in Fig. 11. In a 10-ton Amsler hydraulic testing machine for loading, spherical seats were used to eliminate the bending moment due to eccentricity. It seems that the values at fracture, such as the fracture loads by the load index of the testing machine and those of strains up to fracture obtained by measuring diameters after fracture, are wanting in accuracy because of the sudden fracture phenomenon. For the above reason, the real instant of fracture was detected by the electrical measurements

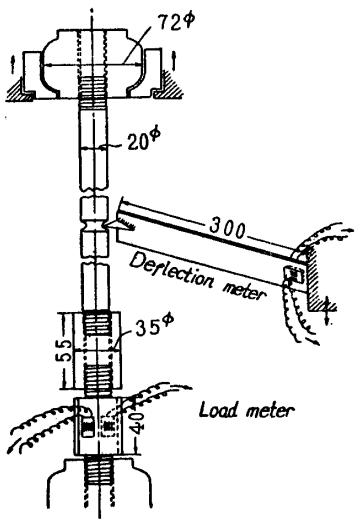

FIGURE 11. Schematic diagram of testing apparatus and procedure.

through the use of resistance wire strain gauges, by which the fracture load and the diameter at the notch section at the instant of fracture were determined. For the former measurement, a mild steel bar of larger diameter in series connection with the specimens was used and for the latter measurement, a thin plate cantilever was used as deflection gauge. The cantilever was set in a deflected state and made vertically movable, so that the top end of cantilever may be always in contact with the notch bottom regardless of its vertical displacement. The deflection is measured from the resistance wire strain gauges bonded on either side of the cantilever near the fixed end.

2.3. TENSILE FRACTURE TEST RESULTS

(1) *Loads (Stresses) and Strains at Fracture*

From the loads (P) and the diameters (d) at notch section measured as described

above, the curves of P versus d_0/d (d_0=initial diameter) are shown in Fig. 12 and the curves of average axial true stress σ_{za} versus average axial logarithmic strain ε_{za} defined as follows, are shown in Fig. 13.

$$\left.\begin{aligned}\sigma_{za}&=P/A=P/\pi a^2,\\ \varepsilon_{za}&=2\ln(d_0/d).\end{aligned}\right\} \tag{13}$$

The diameters of notch section at the moment of fracture and after fracture are compared as compiled in Table 2. The differences between these two values are

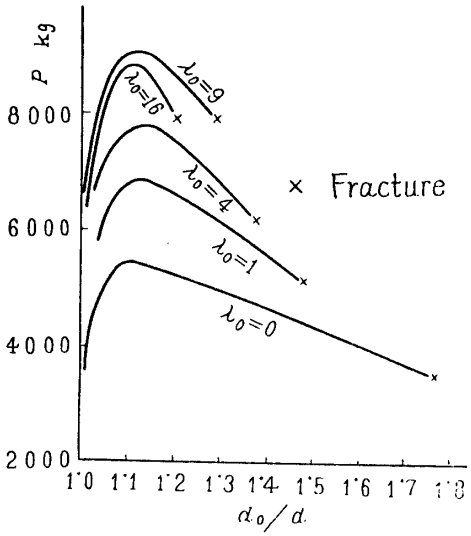

FIGURE 12. Flow curves of loads versus diameters in notch section.

TABLE 2. DIFFERENCE OF DIAMETER OF NOTCH SECTION BETWEEN AT MOMENT OF FRACTURE AND AFTER FRACTURE

Type	Diameter (mm)		$\frac{\Delta d}{d_f}=\frac{d_f-d_a}{d_f}$ (%)
	at moment of fracture, d_f	after fracture d_a	
(0)	6.67	6.56	1.65
(i)	7.98	7.71	3.38
(ii)	8.71	8.14	6.54
(iii)	9.64	9.37	2.80
(iv)	10.17	—	—

unexpectedly great, especially in the intermediate (ii) type of specimen. This may be attributable to the reason that, when the fracture begins at the center or at the notch bottom, additional stretching occurs at the notch bottom or at the center, respectively, as fracturing proceeds. Moreover, as the notch sharpness $\lambda_0=a_0/\rho_0$ increases, the fracture, after the maximum load is reached, occurs suddenly and tends to embrittle metals. Therefore, the fracture loads measured by the electrical devices differ from those measured by load index of the hydraulic testing machine according to the time lag in abrupt fall of load just before fracture. The calculations of fracture stresses and strains due to the radius after fracture and the load

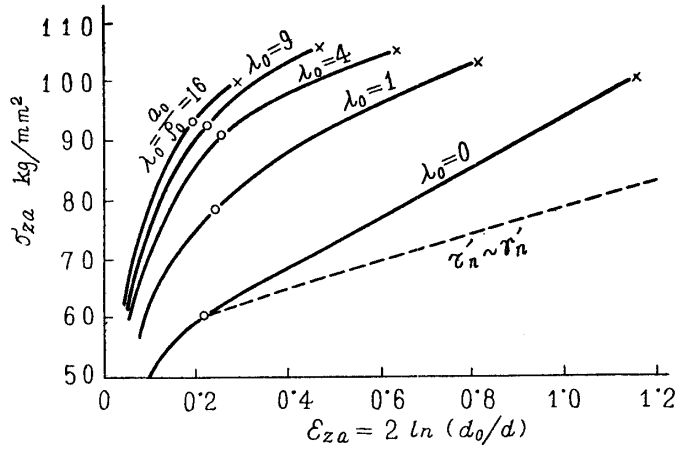

FIGURE 13. Flow curves of average axial true stresses versus average axial logarithmic strains.

index of the testing machine would lead to their inexact values.

The stresses σ_{zm} and σ_{zr}, the strains ε_{zm} and ε_{zr} (suffixes "m" and "r" denote the instant of maximum load and fracture, respectively) are plotted against λ_0 in Fig. 14. The yield stress decreases with increasing notch sharpness because of the stress concentration [*23*] [*24*], while the load P_r and P_m increase on the contrary

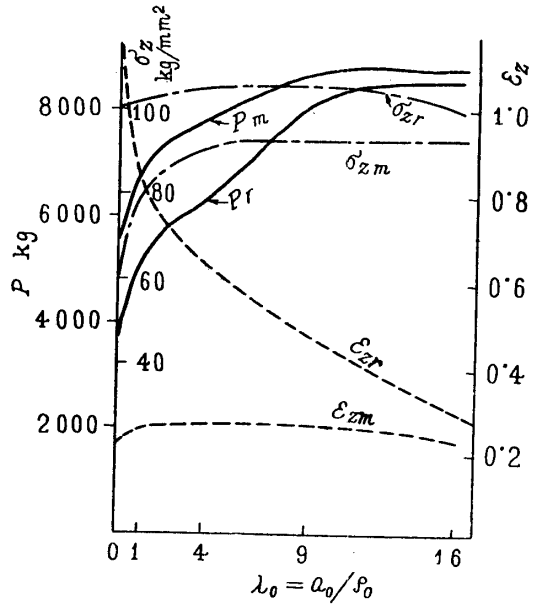

FIGURE 14. Variations of loads, stresses and strains at maximum load and at fracture with notch sharpness.

because of the elastic constraint of a comparatively large volume on either side of the notch. The fracture stress σ_{zr} has a maximum value at $\lambda_0=9$ and, further, tends to decrease with the increase of the notch sharpness.

The contraction of minimum cross section will now be considered. λ_0 causes no difference in ε_{zm}; however, ε_{zr} decreases with increasing λ_0, showing a tendency toward notch brittleness.

(2) *Behaviors of Fracture Surfaces and Locations of Initial Fracturing*

The figures of specimens sectioned along the longitudinal axis after fracture are shown in Photograph 1.

For unnotched specimens, the fracture surfaces present the well-known cup-and-cone behaviors and the starting point of fracture is on the center as previously indicated by the X-ray or other methods. On the other hand, for sharply notched specimens, the fracture surfaces present nearly horizontal cleavage behavior, and the fractures start clearly from the notch bottom. For specimens having intermediate sharpness, for instance in the type of (iii) ($\lambda_0=9$), it is impossible to distinguish between the kinds of fracture and there are samples in which the fracture seemed to start from the intermediate range between both extremes. The boundary at which the fracture stress begins to decrease because of notch brittleness with the increase of notch sharpness seems to correspond to the change of the starting point of fracture from center to notch bottom. This can be also observed in Brown's experiment on mild steel [*25*] and Dana's experiment on duralumin [*26*]. The color of fracture surface is grayish-black, and considerable plastic deformation on the whole for less sharply notched specimens is shown; while, for sharply

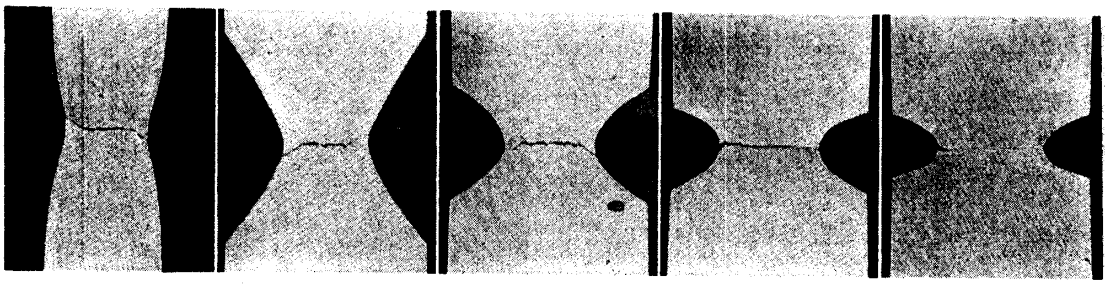

(0) $\lambda_0=0$ (i) $\lambda_0=1$ (ii) $\lambda_0=4$ (iii) $\lambda_0=9$ (iv) $\lambda_0=16$

PHOTOGRAPH 1. Figures sectioned along the longitudinal axis after fracture.

notched specimens, only the outer part of the fracture section has grayish-black color, and the remaining central part has gray-white color which shows that the plastic deformation is restricted to the notch bottom.

(3) *Surface Contour Radius at Fracture*

The notch sharpness $\lambda=a/\rho$ (a=radius of notch cross section at fracture, ρ= contour radius of notch bottom at fracture) necessary for analysing the stress and strain distributions will now be considered.

The initial configuration of surface contour at notch bottom before test is a hyperbola shown by

$$(x/a_0)^2-(y/b_0)^2=1\,. \tag{14}$$

Then the notch sharpness λ_0 can be defined by the following expression.

$$\lambda_0=a_0/\rho_0=(a_0/b_0)^2\,. \tag{15}$$

The configuration after fracture is not hyperbolic as shown in Photo. 1 and the true configuration at fracture moment is presumed by correcting the configuration

after fracture and by taking into account the radius at the notch cross section measured by electrical devices. The corrected configuration of surface contour is assumed to be a hyperbola approximately at each point on the surface contour, and (a/b) is calculated by the following equation after measurment of (y/a) against (x/a).

$$a/b=\sqrt{(x/a)^2-1}\cdot(a/y)\,. \tag{16}$$

The apparent notch sharpness λ can be defined as $\lambda=(a/b)^2$ according to Eq. (15) and the distributions of λ along the surface contour are plotted against (x/a) in Fig. 15. By exterpolating each curve to the ordinate $(x/a=1)$, λ at the notch bottom

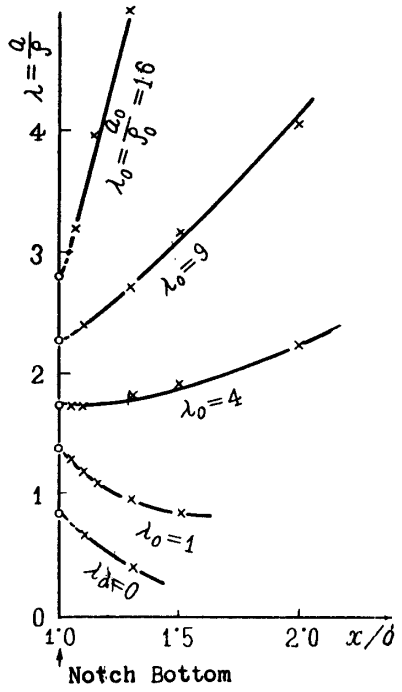

FIGURE 15. Distributions of apparent notch sharpnesses along the distance from notch bottom.

can be determined, and the variations of λ at the notch bottom are as compiled in Table 1. It will be seen from Fig. 15 that the curvature of surface contour increases towards the notch bottom in (i) type of specimen, presenting the necking phenomenon is a manner similar to that of (0) type of unnotched specimen. As the notch becomes sharper, however, the curvature of surface contour decreases towards the notch bottom, indicating that the axial plastic deformation occurred at the notch bottom.

2.4. Approximate Analysis of Stress and Strain Distributions Across the Minimum Notch Section at Fracture

The values which can be determined directly from notch tensile tests are only the average values of axial stress and strain over the notched or necked section.

This is one reason why the explanation of notch brittleness is merely qualitative and not sufficiently quantitative.

The stress distributions in a necked cylindrical bar have been analysed so far by Siebel [*27*], Bridgman [*28*], Davidenkov [*29*] and Aronofsky [*30*] etc., under the assumption that the axial strain ε_z is uniform and the tangential strain ε_t equals the radial strain ε_r over the entire cross section. However, because the contour

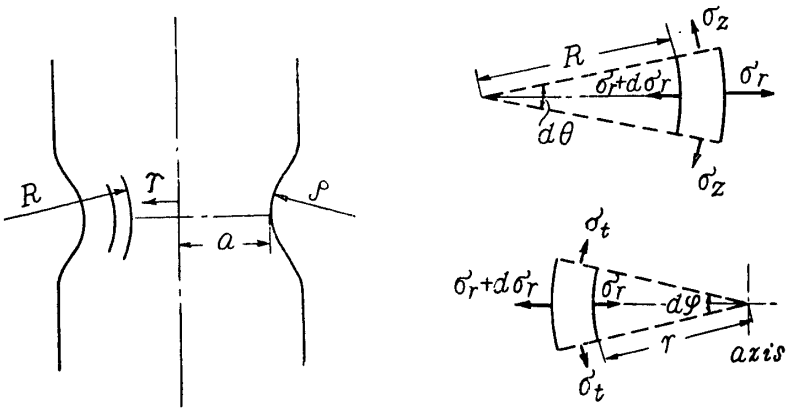

FIGURE 16. Equilibrium of stresses in the neighbourhood of notch.

of the neck is developed by the strain itself, while the strain distribution in a notched specimen is governed by the contour of the notch, these conclusions can not be applied to sharply notched specimens. For this reason, the author analysed the stress and strain distribution across the minimum notch section approximately by extending the Davidenkov's method.

(1) *Equilibrium Equation*

The following will be restricted to the notch section, and the equilibrium condition of stresses in an element along the trajectories of principal stresses as shown in Fig. 7 will be considered, τ_{rz}, $\partial\sigma_z/\partial z$ being neglected as infinitesimal quantities. The neglecting of the small quantities in the following equilibrium equation

$$-(\sigma_r+d\sigma_r)Rd\theta(r+dr)d\varphi+\sigma_r(R+dr)d\theta\cdot r\cdot d\varphi$$
$$-\sigma_z dr(r+dr/2)d\varphi\cdot d\theta+\sigma_t dr(R+dr/2)d\theta\cdot d\varphi=0,$$

finally leads to the following equation.

$$\sigma_z=\sigma_r[1-(R/r)]-(d\sigma_r/dr)R+\sigma_t R/r\,. \tag{17}$$

The radius of curvature of fiber along the axial principal stress (R) is assumed to be

$$R=(a/r)^n\rho \tag{18}$$

across the minimum section of the notch. n nearly equals 1 in the case of $\lambda_0=0$ as assumed in the previous papers. However, n will take gradually larger values with increasing notch sharpness. In this analysis, the following values of n for each type of notched specimen are used for convenience in analysis.

for the (0) type $\cdots\cdots$ $n=1$,
„ (i) type $\cdots\cdots$ $n=3/2$,
„ (ii)~(iv) types $\cdots$ $n=2$.

Then, the equilibrium equation in Eq. (17) can be written as follows, respectively:

$$\left.\begin{aligned}
&\sigma_z=\sigma_r+(\sigma_t-\sigma_r)/\lambda\zeta^2-(1/\lambda\zeta)d\sigma_r/d\zeta \quad \cdots \text{ for the (0) type,}\\
&\sigma_z=\sigma_r+(\sigma_t-\sigma_r)/\lambda\zeta^{\frac{5}{2}}-(1/\lambda\zeta^{\frac{3}{2}})d\sigma_r/d\zeta\cdots \quad \text{„ (i) type,}\\
&\sigma_z=\sigma_r+(\sigma_t-\sigma_r)/\lambda\zeta^3-(1/\lambda\zeta^2)d\sigma_r/d\zeta \quad \cdots \quad \text{„ (ii)~(iv) types,}
\end{aligned}\right\} \tag{19}$$

where $\lambda=a/\rho$, $\zeta=r/a$.

(2) *Compatibility Equation*

Let "u" denote the radial displacement. The natural strains ε_r and ε_t can be defined as

$$\left.\begin{aligned}
&\varepsilon_r \text{ (radial natural strain)}=\ln(1+du/dr),\\
&\varepsilon_t \text{ (tangential natural strain)}=\ln(1+u/r).
\end{aligned}\right\} \tag{20}$$

Eliminating u from both equations in Eqs. (20), we obtain the following compatibility equation

$$e^{\varepsilon_r-\varepsilon_t}=1+(d\varepsilon_t/d\zeta)\zeta. \tag{21}$$

(3) *Condition of Volume Constancy*

The condition of constancy of material volume during the plastic deformation can be written as

$$\varepsilon_r+\varepsilon_t+\varepsilon_z=0. \tag{22}$$

(4) *Stress versus Strain Relation*

Based on "the plastic deformation theory", we use a strain hardening function expressed by the octahedral shear stress τ_n and the octahedral shear strain γ_n as stress versus strain relation, in which the effects of anisotropy and loading process are neglected. For convenience of correlating it to the simple tensile test, τ_n' and γ_n' obtained by correcting the constant terms in τ_n and γ_n are used as follows.

$$\left.\begin{aligned}
&\tau_n'=\sqrt{(\sigma_r-\sigma_t)^2+(\sigma_t-\sigma_z)^2+(\sigma_z-\sigma_r)^2}/\sqrt{2},\\
&\gamma_n'=\sqrt{(\varepsilon_r-\varepsilon_t)^2+(\varepsilon_t-\varepsilon_z)^2+(\varepsilon_z-\varepsilon_r)^2}\cdot\sqrt{2}/3.
\end{aligned}\right\} \tag{23}$$

Putting $\beta=\tau_n'/\gamma_n'$, the equations between stress and strain components can be written as follows by taking into account Eq. (22)

$$\left.\begin{aligned}
&\beta\varepsilon_r=\{\sigma_r-(\sigma_t+\sigma_z)/2\},\\
&\beta\varepsilon_t=\{\sigma_t-(\sigma_z+\sigma_r)/2\},\\
&\beta\varepsilon_z=\{\sigma_z-(\sigma_r+\sigma_t)/2\}.
\end{aligned}\right\} \tag{24}$$

The relation of τ_n' versus γ_n' for plastic flow can be obtained from the flow curve in an unnotched specimen. It is natural that

$$\tau_n'=\sigma_{za},\quad \gamma_n'=\varepsilon_{za} \tag{25}$$

before the neck develops. However, after necking, the state of triaxial stress is produced, resulting in

$$\tau_n'=\sigma_{za}/(1+\lambda/4), \quad \gamma_n'=\varepsilon_{za} \tag{26}$$

according to the correction by Davidenkov. Bridgman [*28*] has given an empirical relationship for λ in terms of ε_{za} after necking as shown by the solid line in Fig. 17,

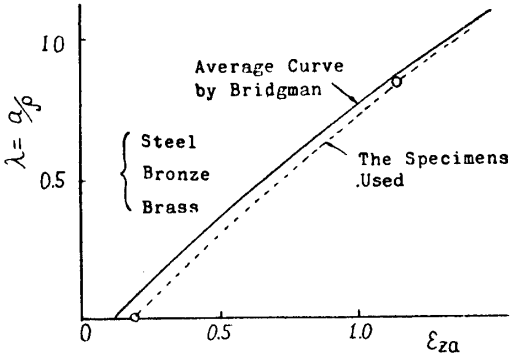

FIGURE 17. Relation between notch sharpness at notch bottom and average axial logarithmic strain.

which is almost similar in many metallic specimens. The author used the relationship for this material as shown in a broken line in Fig. 17, after correction by taking into consideration the datum at the moments of maximum load and fracture obtained in this experiment.

(5) *Boundary Conditions*

The average axial stress σ_{za} can be written by

$$\sigma_{za}=P/\pi a^2=2\int_0^1 \sigma_z \zeta d\zeta \tag{27}$$

and the boundary conditions for stresses in the minimum cross section are

$$(\sigma_r)_{r=a}=0, \quad (\sigma_r)_{r=0}=(\sigma_t)_{r=0}=\sigma_0 . \tag{28}$$

On the other hand, the following relationship between ε_{za} and ε_{t1}

$$\varepsilon_{za}=-2\varepsilon_{t1} \tag{29}$$

(suffix "1" denotes the surface) can be obtained by eliminating u_1/a from the following two equations due to Eqs. (13) and (20).

$$\varepsilon_{za}=\ln (a_0/a)^2=2\ln [a_0/(a_0+u_1)] ,$$
$$u_1=a_0(e^{\varepsilon_{t1}}-1) .$$

(6) *Analysis of Stress and Strain Distributions*

For the unnotched specimens, we utilize the analytical results of Davidenkov concerning to stress distributions as they stand. However, for the notched specimens, we consider as follows.

First of all, σ_r is assumed as expressed in Eq. (30) by referring to the boundary conditions of Eq. (28) and by adding the correction term (the third term in the right-hand side in Eq. (30)) into the solution obtained when $\sigma_t=\sigma_r$ is assumed in

Eq. (19) under the consideration that the stress distribution will approach the elastic one because of the existence of the notch.

$$\left.\begin{aligned}\sigma_r/\sigma_0&=1-\zeta^{\frac{5}{2}}+\gamma\zeta^{\frac{5}{2}}(1-\zeta^2)\cdots \text{ for the (i) type,}\\ \sigma_r/\sigma_0&=1-\zeta^3+\gamma\zeta^3(1-\zeta^2)\cdots \quad \text{,, (ii)}\sim\text{(iv) types.}\end{aligned}\right\} \tag{30}$$

Similarly, σ_t is also assumed as expressed in Eq. (31) by taking into account the occurrence of tangential tensile stress on the notch bottom.

$$\left.\begin{aligned}\sigma_t/\sigma_0&=\sigma_r/\sigma_0+\alpha\zeta^{\frac{5}{2}}\cdots \text{ for the (i) type,}\\ \sigma_t/\sigma_0&=\sigma_r/\sigma_0+\alpha\zeta^3\cdots \quad \text{,, (ii)}\sim\text{(iv) types.}\end{aligned}\right\} \tag{31}$$

Then, σ_z can be obtained from Eq. (19) as follows.

$$\left.\begin{aligned}\sigma_z/\sigma_0&=1-\zeta^{\frac{5}{2}}+\gamma\zeta^{\frac{5}{2}}(1-\zeta^2)+\alpha/\lambda+5/2\lambda-\gamma(5-9\zeta^2)/(2\lambda)\\ &\qquad\cdots \text{ for the (i) type,}\\ \sigma_z/\sigma_0&=1-\zeta^3+\gamma\zeta^3(1-\zeta^2)+\alpha/\lambda+3/\lambda-\gamma(3-5\zeta^2)/\lambda\\ &\qquad\cdots \text{ for the (ii)}\sim\text{(iv) types.}\end{aligned}\right\} \tag{32}$$

For approximate analysis of the stress and strain distributions, there are two processes, that is, one starting from the axial average fracture stress σ_{zr} and the other starting from the axial average fracture strain ε_{zr}. Here, the former one will be adopted as follows.

First, the values of λ at the notch bottom in each type of notch are determind as shown in Table 1. If appropriate values of γ and α are assumed, then σ_z/σ_0 is obtained together with σ_r/σ_0 and σ_t/σ_0, thus σ_0 can be obtained by Eq. (27). Then, after determination of the distribution of τ_n', that of β across the notch cross section can be obtained from the curve of τ_n' versus γ_n'. Next α is corrected so that the distribution of ε_t due to Eq. (24) may agree nearly with the following distribution of ε_t due to the compatibility equation,

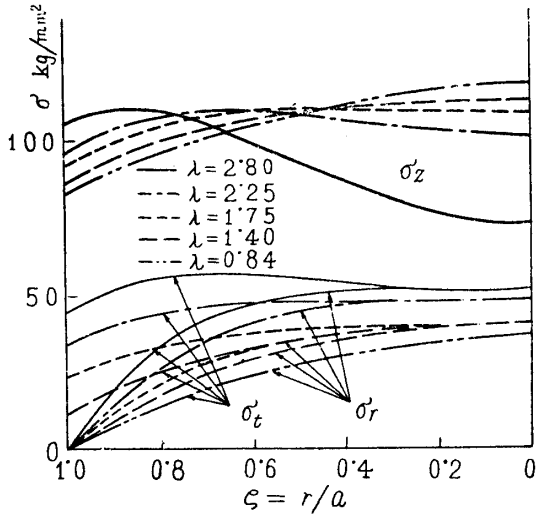

FIGURE 18. Distributions of σ_r,σ_t and σ_z across the notch section.

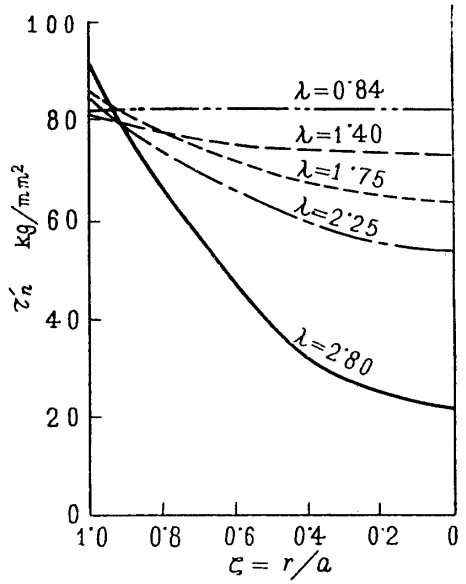

FIGURE 19. Distributions of τ_n' across the notch section.

$$\varepsilon_t=\varepsilon_{t0}+\int_0^1\{e^{3(\sigma_r-\sigma_t)/2\beta}-1\}d\zeta/\zeta \tag{33}$$

and γ is corrected so that the value of ε_{t1} may nearly agree with that due to Eq.(29). By repeating the above processes, finally the converged distributions of stresses and strains can be approximately obtained. The distribution curves for σ, τ_n' and ε_z between the notch bottom and the axis of bar, thus evaluated for each value of

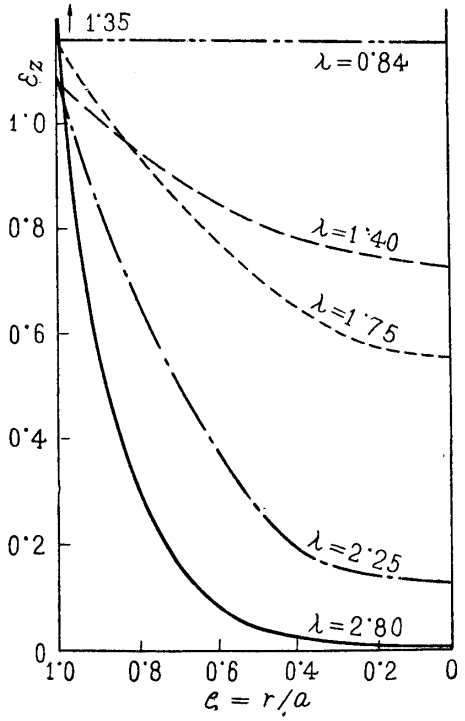

FIGURE 20. Distributions of ε_z across the notch section.

λ, are shown in Figs. 18, 19 and 20, respectively. In the above analysis, the appropriate values of n are conveniently assumed for analysis, therefore it will be supposed that these distributions are not exactly equal with the true distributions, but at least approach these, and the true distributions will be given by the complex functions of n and ζ.

(7) *Comparison of the Stress and Strain Distributions and the Fracture Behaviors*

The distributions of stresses tend to approach the elastic one with the increase of notch sharpness, resulting in embrittleness, and the plastic deformations occur chiefly at the notch bottom. The fracture surface of a sharply notched specimen presents a circular distinction line in color between outer and inner parts in the minimum notch cross section as already described in Section 2.3 (2). The value of τ_n' on the line where the color changes abruptly corresponds to that of τ_n' in the flow curve of τ_n' versus γ_n' in Fig. 13 where γ_n' increases abruptly. The gray-black color of almost the entire cross section in types (0), (i) and (ii) can be attributed to the large values of τ_n' over the entire area.

2.5. Explanation of Notch Brittleness by the Fracture Criterion Proposed by the Author

The above tensile fracture tests of notched specimens will be explained by the fracture criterion proposed in Part I. The gradients of plastic stress distributions are not so sharp as in the elastic state. Therefore, the fracture criterion in which the effects of stress gradient are neglected can be applied to each point on the entire cross section. Based on the stress distributions at fracture just analysed above, the maximum shear stress τ_m and the maximum tensile stress σ_m on each point on the minimum cross section are plotted against θ at that point in Fig. 21 in fine and bold-face curved lines, respectively. The values shown in parentheses at the right and left ends of each curve denote the values of τ_n' at fracture on the center and at the notch bottom, respectively.

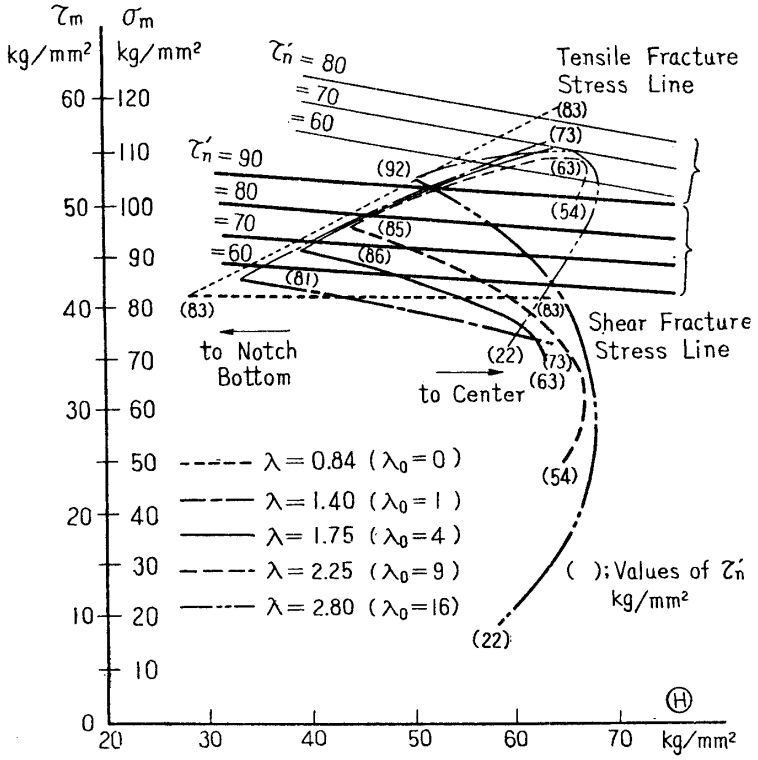

FIGURE 21. Diagram for interpretation of fracture behaviors and notch brittleness.

Both of the fracture stress surfaces, and hence of the fracture stress curves corresponding to each value of τ_n' or γ_n' have not been determined quantitatively by the fundamental polyaxial stress fracture tests on this material. Therefore, the assumed tensile and shearing fracture stress curves for each value of τ_n' are also shown against θ by continuous fine and heavy straight lines, respectively, in Fig. 21. Such assumed fracture stress curves are consistent with the experimental results previously obtained. The intersection point of the σ_m or τ_m curves and the σ_{cr} or τ_{cr} curves, respectively, under the condition of the same value of τ_n', indicates the

fracture stress and the location of initial fracturing. The fracture will be initiated in either of cleavage or shear fracture type according to whichever intersection will be achieved earlier.

For less sharply notched specimens, the maximum tensile stress σ_m at the center is very large under high hydrostatic tension Θ due to the triaxial tensile stress state. Consequently, the σ_m curve first of all comes in contact with the σ_{cr} curve in the range of larger Θ. Thus the cleavage fracture first occurs at the center. The tensile stresses across the cross section decrease from center to periphery, while the shear stresses increase, on the contrary, causing the growth of shear fracture toward the center, which would be expected to result in the formation of the cup-and-cone type fracture surface. Orowan [*31*] asserted that the ductile tensile fractures should not be governed by the maximum tensile stress criterion in the case of the tensile tests of specimens having various grades of notches. Of course, the maximum tensile stress criterion based on the average tensile stress in the fractured cross section would not be consistent with the experimental evidences as shown by the author's experiments. However, if it is corrected by the effects of γ_n and Θ, and applied to each point on the fractured cross section after analysis of the stress and strain distributions, then such a maximum tensile stress criterion will be useful. The fact that the tensile fracture is initiated at the center under high hydrostatic tension is convincing with reference to the Photograph 1. The cup-and-cone type fracture surface presenting a discontinuous boundary may be attributed to the coexistence of two modes of fracture.

For sharply notched specimens, the stress distribution at fracture approaches the elastic one under small plastic deformation, for which the shear stress at notch bottom is large due to the stress concentration. Under these circumstances, the τ_m curve first of all comes in contact with the τ_{cr} curve, the shear fracture first ocurring at the notch bottom. The shear stresses along the cross section decrease suddenly from the notch bottom to the center, while the tensile stresses, on the contrary, increase, causing the propagation of tensile fracture to the central part. In this case, it may be considered that the cleavage brittle fracture is promoted by the concentrated tensile stress at the tip of crack produced by the initial shearing slip. The shear fracture range at the notch bottom presenting oblique ductile fracture surface is so small that a flat cleavage tensile fracture can be seen across almost the entire remaining fracture surface.

For the intermediate specimen of (iii) type ($\lambda_0=9$), the behavior intermediate between the above two behaviors can be seen; that is, either of them occurs, or the fracture seems to start from the intermediate point between center and notch bottom. The latter behavior seems to result from the greatest value of σ_m in the intermediate range and the contact with the σ_{cr} curve.

From the above description, the notch brittleness phenomenon can be expressed as follows. The triaxial stress state is firstly produced by the existence of the notch. However, the plastic deformation in the central part is small because of the decrease of τ_n, especially for sharp notches, introducing the stress concentration at the notch bottom as in the elastic state. So the shear fracture starts at notch

bottom in a limited range and, further, the tensile fracture propagates to the center rapidly, when there is no time to spare for the plastic deformation. In fact, in the brittle fracture of all-welded ships, there has been seen the presence of a thin plastically deformed layer at the notch bottom, from which the crack originates. The decrease of the energy absorbed in a notched specimen with increasing the notch sharpness is considered to be due to the larger percentage of area of fractured surface caused by the cleavege fracture, and it is worthy of note that the major type of fracture dominating the cross section is different from the type of fracture as the cause of initiating the fracture. The greatest value of fracture stress in the intermediate (iii) type as shown in Fig. 14 appears to result from the absence of both extreme possibilities of cleavage fracture at the center for less sharp notches and of the shear fracture at the notch bottom for sharp notches.

The problem of propagation of a crack after initiation of fracture is a dynamic one accompanying the rapid change of stress distribution and there is a need for further rigorous study on the propagation of cracks. The above interpretations concerning the fracture behavior should not be concluded as completely reasonable, but it appears to agree, in part at least, with the start of fracture.

Part III. Deformation and Fracture of Gray Cast Irons under Combined Stress

3.1. Introduction

The author has, in order to ascertain the validity and applicability of his criterion to brittle metals, carried out fracture tests on thin-walled gray cast iron tubes under various ratios of combined tension and torsion loads. The author made these experiments with due consideration of the intrinsic importance attached to the fracture occurring in brittle metals and the significance, which these experiments would offer in the study on the fracture criterion, in view of the greater assurance of determining the state of stress at fracture and reduction of the strain-hardening in brittle metals by virtue of their limited ductility and absence of the necking phenomenon. Moreover, the use of thin-walled tube specimens subject to combined tension and torsion loads offers an approximate stress state, which eliminates the effect of a stress gradient. Gray cast iron, although inherently of heterogeneous polyphase structure was selected as a typical brittle metal common in the engineering field.

Division A describes the deformation behavior before fracture. The peculiarities arising in elastic and plastic deformations under combined stresses and absent in ductile metals are discussed with due account of the notch effect due to the heterogeneous graphites in the pearlite matrix.

Division B deals with the discussion on the fracture behavior by taking into account the mechanism of deformation as proposed by Fisher and application of the fracture criterion at the tip of the graphite flake. Lastly, the findings of other research students related to the study of fracture under other kinds of polyaxial

stresses are cited and discussed for the purpose of analyzing the criteria proposed by others.

3.2. Test Procedure

(1) *Specimens*

Gray cast iron specimens used in this study were carefully produced in the form of cylindrical bars (30 mm in diameter and 150 mm in length) to eliminate blow-hole or foreign inclusions as much as possible. The chemical composition of the material was as follows:

C 3.25% (graphite carbon 2.3%, combined carbon 0.95%),
Si 1.85%, Mn 0.62%, P 0.090%, S 0.106%.

Photograph 2. Microphotograph of metallurgical structure of this material, at 150× magnification.

The cast iron was cooled slowly after casting and most of the carbons were mostly included in the form of graphite flakes. A microphotograph of the metallurgical structure is shown in Photo. 2.

(a) Specimens for tension and torsion and combined tension and torsion.

Specimens were machined from bars into thin-walled tubes as shown in Fig. 22 (a) by removing the central and peripheral parts of the bars so as to produce specimens of comparatively uniform structure. Two specimen sizes were used in which the diameters (d_i) were as follows:

Type I: $d_i=12$ mm; Type II: $d_i=13$ mm.

The deformation data in Division A relate to Type I specimens, and the fracture data given in Division B relate to both types of specimens.

(b) Specimens for compression.

The specimens used for compression were solid prisms having a square cross section as shown in Fig. 22 (b). These specimens were tested in the as-cast condition.

(2) *Testing Machine and Test Procedure*

Specimens were loaded with a testing machine as shown in Fig. 23 which is an Olsen universal testing machine modified for biaxial stressing with the addition of an apparatus for torsional loading. The tensile load is applied by pulling down ① on the machine, while torsional loading is applied by rotation of a handle ④ actuating a worm gear ③, both being mounted on a vertically movable block

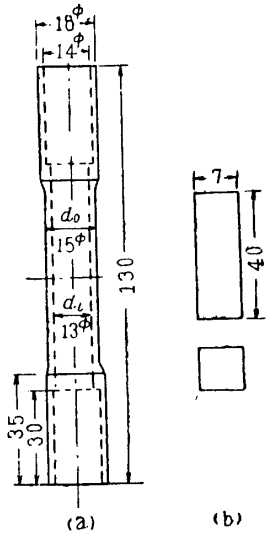

FIGURE 22. Test specimens (a) for combined tension and torsion (b) for compression.

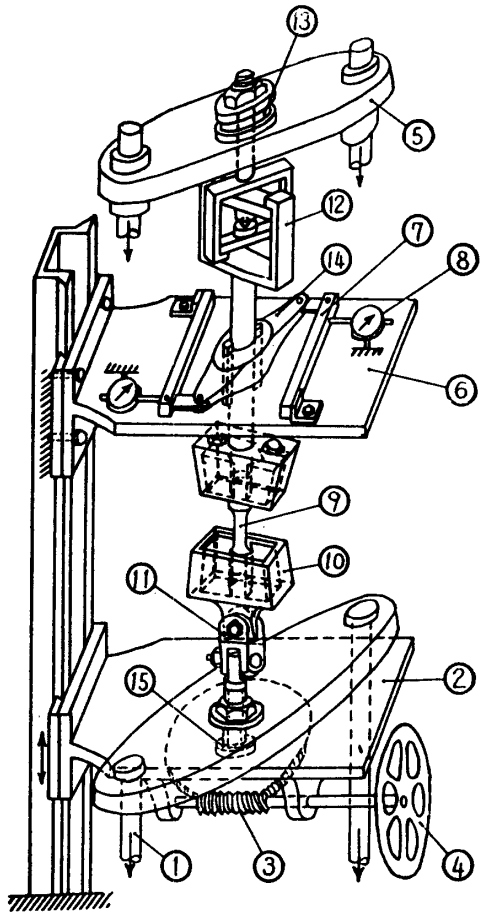

FIGURE 23. Schematic diagram of testing machine and for explanation of testing procedure.

supported by a thrust ball bearing ⑮. A block ⑤ supported by a thrust bearing is pulled down by a tensile load, the amount of displacement being measured by a lever type apparatus on the machine. The torsional load is transmitted as tip loads on two cantilevers ⑦ through an arm ⑭ mounted on a fixed block ⑥, the amount of torque being measured as the sum of the deflections of two dial gauges ⑧ after calibrations. Both ends of a specimen ⑨ are grasped by grips provided with conventional V grooves and the grips totally enclosed grip holders ⑩. The swivels ⑪ and ⑫ serve to eliminate the bending moment due to eccentricity. The torsional moment resulting from the friction in the thrust ball bearing under tensile loading and the factor of tensile load arising from the friction between the plane of contact between ⑭ and the shaft resulting from the application of a torsional moment were duly considered, but these factors were, upon precise calibration, neglected because of their negligible magnitude. The tensile load (P) and the torsional moment (T) were applied in a manner such that the ratio of tensile stress (σ) to shear stress (τ) would be maintained constant in biaxial plane stress in the tube. The principal tensile stress (σ_1) was adjusted and applied at a rate of 1.8 kg/mm^2/min.

The compression load was applied with a 10-ton Amsler hydraulic testing machine.

(3) *Estimation of Stresses*

As the strains up to the point of fracture are small, the tensile stresses are defined by nominal stresses based on the original cross section and in accordance with the following equation.

$$\sigma=4P/\pi(d_o^2-d_i^2) \tag{34}$$

where d_o, d_i=outer and inner diameters of tube respectively.

The shear stress is non-uniform along the radius; the average shear stress (τ) is taken as the shear stress, because the wall of the tube is thin and a considerably uniform stress distribution is obtained during plastic deformation. The shear stress can be defined according to Eq. (35) from $T=\tau\int_{r_i}^{r_0}2\pi r\cdot r\cdot dr$

$$\tau=12T/\pi(d_o^3-d_i^3)\,. \tag{35}$$

The equations for the two principal stresses σ_1 and σ_2 ($\sigma_1>\sigma_2$) are given as follows.

$$\sigma_1=\{\sigma+\sqrt{\sigma^2+4\tau^2}\}/2\,,\quad \sigma_2=\{\sigma-\sqrt{\sigma^2+4\tau^2}\}/2\,. \tag{36}$$

The experiments were carried out by maintaining the following stress ratios constant.

$$\xi=\sigma_2/\sigma_1\,,\quad \text{or}\quad \lambda=\tau/\sigma\,. \tag{37}$$

Table 3 gives the five values of ratio used in the experiments.

TABLE 3

ξ	0	−1/4	−2/4	−3/4	−1
λ	0	2/3	$\sqrt{2}$	$2\sqrt{3}$	inf.
	Simple tension	Combined tension and torsion			Simple torsion

(4) *Measurement of Strains*

In the tests of ξ ranging from 0 to −1, mirror extensometers were employed in measuring the tensile axial strain (ε_a) and the shearing strain (γ) as the strains involved are of small magnitudes. γ is defined as the value at mid-thickness which corresponds to the use of the average shear stress. The average cirumferential strain (ε_t) and the average radial strain (ε_r) are defined by Eq. (38) and determined by substituting values measured with resistance wire strain gauges bonded circumferentially on the outside and inside of the tube.

$$\left.\begin{aligned}\varepsilon_t&=(\varepsilon_{to}+\varepsilon_{ti})/2\,,\\ \varepsilon_r&=(\varepsilon_{to}d_o-\varepsilon_{ti}d_i)/(d_o-d_i)\,.\end{aligned}\right\} \tag{38}$$

The subscripts "o" and "i" in the above equations refer to the outside and inside of a tube respectively.

In the compressive tests, both ε_a and $\varepsilon_t(\varepsilon_r)$ were measured by means of resistance wire strain gauges.

Division A: Deformation Behaviors under Combined Stresses

3.A.1. Experimental Results on Deformations in Tension and Compression and Their Considerations

(1) *Stress and Strain Diagrams*

Typical stress (σ) versus strains (ε_a, ε_t) curves under tensile loading are shown in Fig. 24. Specimens were unloaded a few times before fracture in order to separate the strain component into their elastic and plastic components as denoted by the subscripts "e" and "p" respectively in the following equations and the elastic component was found by the restoring amount.

$$\varepsilon_a=\varepsilon_{ae}+\varepsilon_{ap}, \quad \varepsilon_t=\varepsilon_{te}+\varepsilon_{tp}. \tag{39}$$

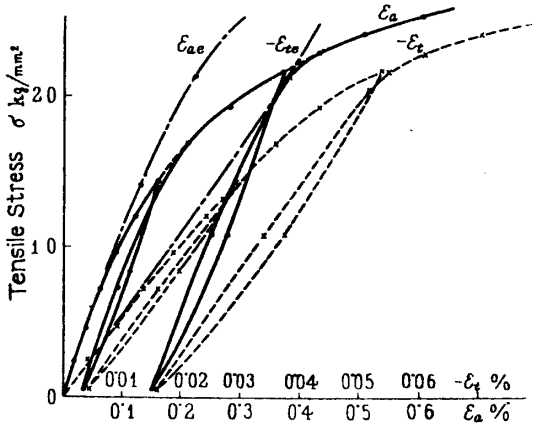

FIGURE 24. Stress versus strains curves under tensile loading.

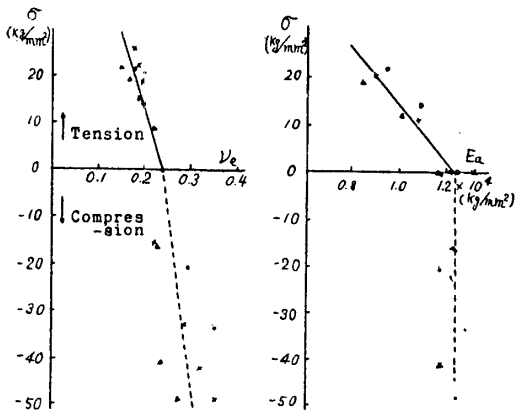

FIGURE 25. Variations of E_a and ν_e under simple uniaxial loading.

First, the elastic strain components will be considered. A marked characteristic is observed especially in tension, i.e., the $\sigma\sim\varepsilon_{ae}$ and ε_{te} relations are non-linear presenting concave and convex curves in the lower part respectively which are phenomena dissociated with ductile metals. If the apparent Young's modulus E_a and elastic Poisson's ratio ν_e are defined by the following equations,

$$E_a=\sigma/\varepsilon_{ae}, \quad \nu_e=-\varepsilon_{te}/\varepsilon_{ae} \tag{40}$$

we will find that E_a and ν_e will not remain constant with variation of tensile stress σ but actually decrease with the increase in tensile stress. The variations of E_a and ν_e in relation to the stress σ under uniaxial stressing are shown in Fig. 25 which can be represented approximatly by the linear equations noted as follows in the tensile and compressive fields respectively.

$$E_a=E_0-\alpha\sigma, \quad \nu_e=\nu_0-\beta\sigma. \tag{41}$$

It is difficult to produce a state of uniform uniaxial compressive stress under compressive loading because of the barelling effect of specimens. Even when these effects are admitted, the increase in both E_a and ν_e with increasing compressive stress seems to be small and especially in E_a. The values of the coefficients α and

β in Eq. (41) under compression are small in comparision with those under tensile loading.

Next, the plastic strain components will be considered. If the plastic Poisson's ratio ν_p is defined by the equation

$$\nu_p = -\varepsilon_{tp}/\varepsilon_{ap}\,, \tag{42}$$

then ν_p will show a variation with increasing tensile stress similarly as found with ν_e and it is found to be considerably less than 0.5 for tension, while it is found to approach 0.5 with increasing compressive stress. The permanent volume change is defined by the following equation.

$$(\Delta V/V)_p = \varepsilon_{ap} + 2\varepsilon_{tp} = \varepsilon_{ap}(1-2\nu_p) \tag{43}$$

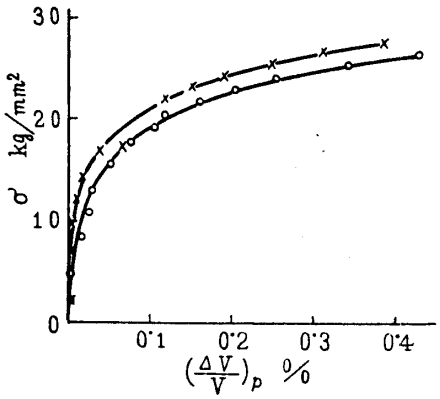

FIGURE 26. Plastic volume change during tensile loading.

The change in volume, for example, in the case of uniaxial tension is shown in Fig. 26. It has been recognized that ν_p is nearly 0.5 at all times with ductile metals subject to plastic deformation and practically devoid of any volume change. While in gray cast irons, we will find that a permanent increase in volume will always occur indicating a violation of the assumption of incompressibility.

(2) *Considerations of Peculiarities in Deformations by Metallurgical Structures of Gray Cast Irons*

A microphotograph of this material after buff-polishing is shown in Photo. 2 which reveals that the dispersed graphite flakes exist in the pearlite matrix thereby preventing the polycrystalline grains from binding with each other. The tensile strength of pearlite is considered to be about 80 to 100 kg/mm^2 while that of graphite is no more than 2 kg/mm^2 [*32*], wherefrom it is deduced that the brittle and friable graphite flakes will first be broken down under comparatively low tensile stress and lead to sharp internal cavities. This deduction can readily be substantiated by referring to the microphotograph (Photo. 3) taken after fracture under tension wherein will be noted the development of a fissure in the graphite flakes oriented normal to the direction of tensile loading.

The graphite flakes are randomly oriented with a length to thickness ratio of about 12 to 1 and are conveniently assumed as flat ellipsoidal cavities for purposes

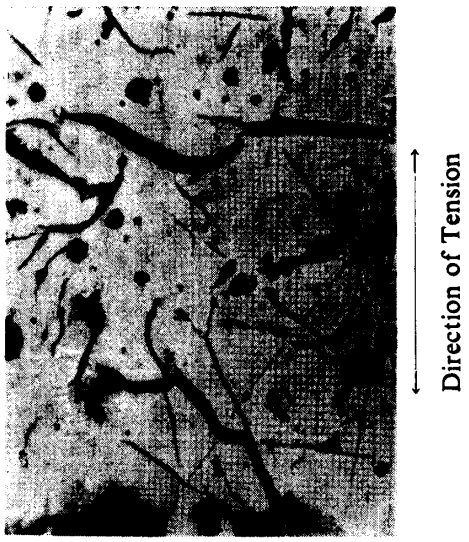

PHOTOGRAPH 3. Fractograph of gray cast irons factured in tensions at 150× magnification.

of analysis. According to the elastic analysis of Sadowski etc. [*33*], the stress concentration factors and displacements around a cavity in an infinite body under uniaxial stress parallel or perpendicular to the axis of revolution are shown in Figs. 27 and 28, respectively. These calculated results, however, cannot be used quantitatively as they stand since they are based on an elastic analysis and because of the fact that the geometrical figures of graphite flakes are different from those in the actual state. Nevertheless, these results will serve to explain the peculiarities of deformation characteristics of cast irons qualitatively. The stress concentration around the equator under uniaxial tension parallel to the axis of revolution of a cavity is very great and a considerable plastic deformation will be restricted to

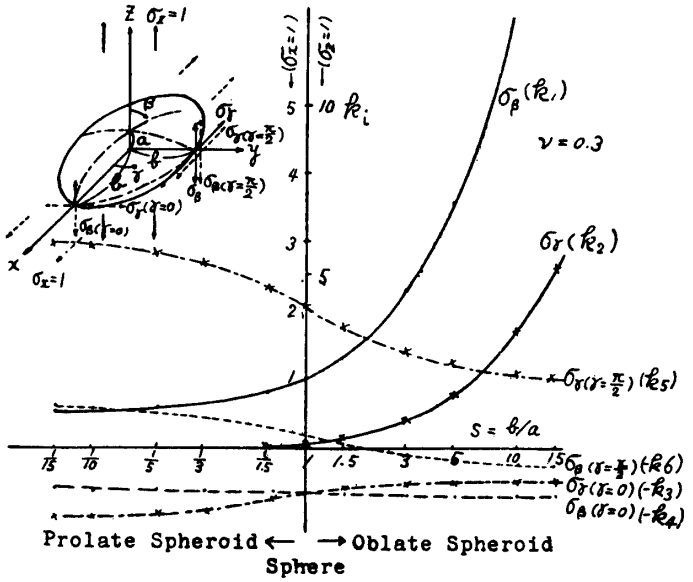

FIGURE 27. Stress concentration factors around an ellipsoidal cavity under uniaxial loading in the direction of its axis.

the tip of a flake as recognized in practice [*34*]. Although the graphite flakes are randomly oriented, it is a fair approximation to assume that only the flakes situated normal to the direction of tensile loading cause the decisive influence on deformation and fracture, while the remaining flakes have little or no effect on the deformation and fracture.

Under tensile loading, the notch sharpness at the edge of oblate flakes normal to tensile stress becomes considerably smaller and the displacement at the pole A (Fig. 28) increases relatively to that at the equator B resulting in the decrease of apparent flatness $s=b/a$. Therefore, the decrease of E_a with an increase in tensile stress can be attributed to the increase of the displacement at the pole $(u_\alpha)_{\beta=0}$ due to the permanent geometrical change of the graphite flakes. Further, the decrease of ν_e can be attributed to the decrease of the ratio; $(u_\alpha)_{\beta=\pi/2}/(u_\alpha)_{\beta=0}$ due to the decrease of s which is shown by the chain line in Fig. 28. The prolate flakes parallel to the direction of tensile loading will not contribute to the variations of E_a and ν_e because of the small stress concentration around the flakes, and therefore, of the small geometrical permanent change. The presentation of a curve under a small stress in the course of initial loading for elastic stress versus strain as evidenced by the experiment can also be satisfactorily explained by the aforenoted considerations.

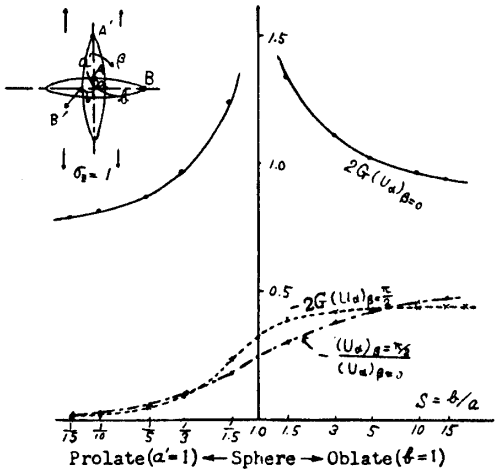

FIGURE 28. Displacements at the pole and the equator of an ellipsoidal cavity under uniaxial loading parallel to the axis of revolution (put the length of its axis equal to 1).

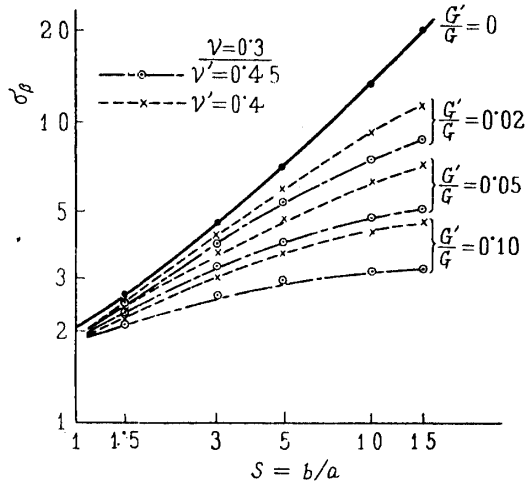

FIGURE 29. Stress concentration factor σ_β at the equator of an ellipsoidal inclusion under uniaxial loading parallel to the axis of revolution.

On the other hand, the compressive strength of graphites is considered to be less than about 10 kg/mm^2 and they will be crushed in compression. However, such graphite flakes will continue to exist as plastic bodies exhibiting little volume change as observed in soils and will not act as cavities. The stress concentration factors (σ_β) at the equator of a flat ellipsoidal inclusion under uniaxial stress parallel to the axis of revolution are analysed and plotted in Fig. 29, with reference to the analysis of Edwards [*35*]. Even in the case where the modulus of shear rigidity of the inclusion G' is much less than that of the pearlitic matrix G, the

stress concentration becomes considerably small in comparison with that in the case of a cavity as the Poisson's ratio of inclusion ν' approaches 0.5. Moreover, the residual tensile stress is expected to occur at the tip of a flake due to the difference in the cofficients of thermal expansion during cooling. Hence, the flakes are not assumed to exert a stress raising effect under compression.

When a flake is subjected to compression, the notch sharpness will somewhat decrease initially because of the restriction of plastic deformation around the edge, while the overall flatness of a flake will be found to increase with an increase in the compressive stress after the flake is crushed. Thus, the change of apparent flatness s will be almost absent or very small even when it occurs. Consequently, the apparent Young's modulus E_a will be almost invariable under compression. The apparent Poisson's ratio ν_e dose not show any appreciable change such as found under tension; however, it does show a tendency to increase slightly with an increase in the compressive stress, which will result from a slight increase in s and with a plastic Poisson's ratio nearly equal to 0.5.

As a result, the author considers that the graphite flakes can transmit compressive stress without a stress raising effect as sound and reliable material, while under tension, it acts as an internal notch, as suggested by Fisher [*36*]. The gray cast irons will present compressive characteristics similar to those associated with ductile materials.

3.A.2. Behavior of Elastic Strain Components under Combined Tension and Torsion

The elastic strain components in the tests under combined tension and torsion were found by maintaining the ratio of biaxial stresses constant and by unloading. The behavior of these components will now be considered.

The apparent Young's modulus E_a and modulus of shear rigidity G_a are expressed by the following equations by using the elastic components of axial strain (ε_{ae}) and shearing strain (γ_e) respectively.

$$E_a=\sigma/\varepsilon_{ae}, \quad G_a=\tau/\gamma_e. \tag{44}$$

The variations in the ratios of E_a/E_0 and G_a/G_0 (E_0 and G_0 denote the values of E_a and G_a near $\sigma=0$ and $\tau=0$ respectively) are shown in Fig. 30 for each value of ξ: E_a and G_a decrease with an increase in the shear stress τ and the tensile stress σ respectively. On the other hand, the modulis of elasticity of ductile materials are independent of the state of stress under combined stress. The unusual variation in gray cast irons will be accounted for as below.

The state of biaxial plane stress under σ and τ can be replaced and reexpressed in terms of the principal tensile stress σ_1 and the principal compressive stress σ_2 according to the following equations as shown in Fig. 31.

$$\sigma_1=\frac{\sigma}{2}(1+\sqrt{1+4\lambda^2}), \quad \sigma_2=\frac{\sigma}{2}(1-\sqrt{1+4\lambda^2}), \quad \tan 2\theta=\frac{2\tau}{\sigma}=2\lambda. \tag{45}$$

Now, the principal strains can be written as

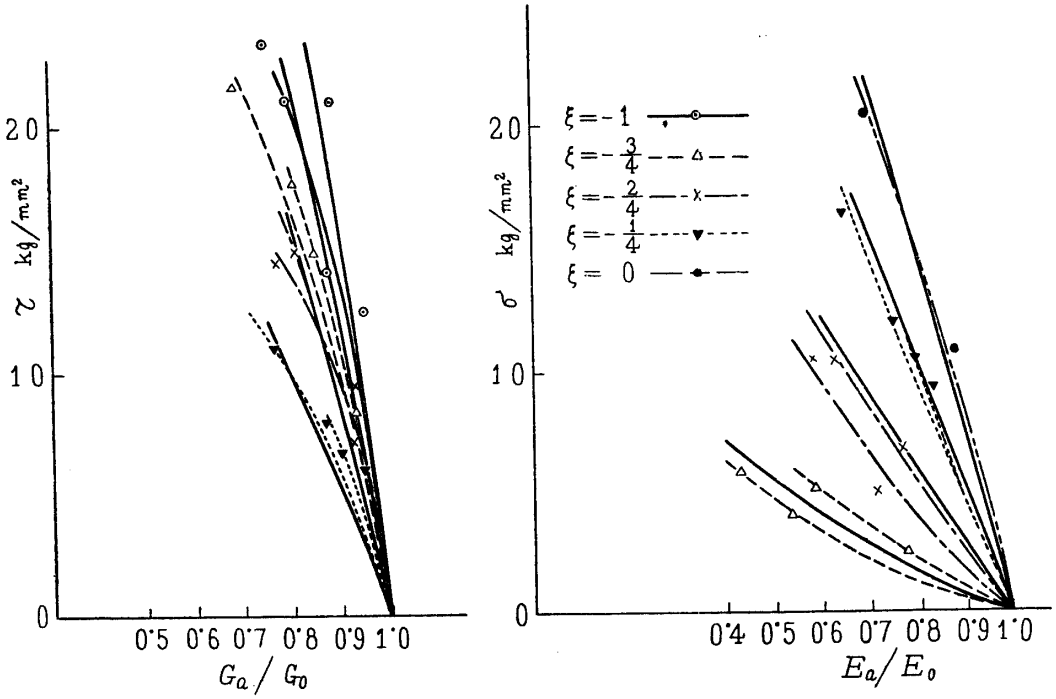

FIGURE 30. Variations of E_a and G_a under combined tension and torsion.

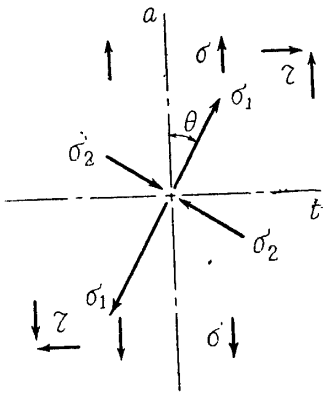

FIGURE 31. Plane stress state under combined tension and torsion.

$$\left.\begin{aligned}\varepsilon_{1e}&=\sigma_1/E_1-\nu_2(\sigma_2/E_2)\,,\qquad \varepsilon_{2e}=\sigma_2/E_2-\nu_1(\sigma_1/E_1)\,,\\ \varepsilon_{3e}&=-\{\nu_1(\sigma_1/E_1)+\nu_2(\sigma_2/E_2)\}\end{aligned}\right\}\tag{46}$$

where, E_1 and E_2 are the tensile and compressive Young's modulis in the directions of σ_1 and σ_2, respectively, and ν_1 ane ν_2 are the Poisson's ratios defined similarly as in the above. These values are expressed as functions of stresses and are assumed to have the same values as under simple uniaxial stresses. This assumption is not true since it must be taken into account the state of stress and the conditions of loading. However, these values will serve convenient for the purpose of analysis in a first rough approximation with the consideration that only the graphite flakes normal to the principal stresses have any decisive effect on the deformation behavior. The reciprocal theorem of Maxwell-Betti will then hold true based on the above presumption.

$$\nu_1/E_1=\nu_2/E_2\,. \tag{47}$$

The elastic strain components in the principal axes of a specimen can be expressed in terms of the principal strains as follows:

$$\left.\begin{aligned}\varepsilon_{ae}&=\varepsilon_{1e}\cos^2\theta+\varepsilon_{2e}\sin^2\theta\,,\\ \varepsilon_{te}&=\varepsilon_{1e}\sin^2\theta+\varepsilon_{2e}\cos^2\theta\,,\\ \gamma_e&=2(\varepsilon_{1e}-\varepsilon_{2e})\cos\theta\sin\theta\,.\end{aligned}\right\} \tag{48}$$

Substituting Eqs. (45) and (46) in Eqs. (48), then Eqs. (48) will be transformed as follows:

$$\left.\begin{aligned}\varepsilon_{ae}&=\frac{\sigma}{2}\left[\left(\frac{1}{E_1}+\frac{1}{E_2}\right)+\frac{1+2\lambda^2}{\sqrt{1+4\lambda^2}}\left(\frac{1}{E_2}-\frac{1}{E_2}\right)\right],\\ \varepsilon_{te}&=\sigma\left[-\frac{\nu_1}{E_1}+\frac{\lambda^2}{\sqrt{1+4\lambda^2}}\left(\frac{1}{E_1}-\frac{1}{E_2}\right)\right],\\ \gamma_e&=\tau\left[\left(\frac{1}{E_1}+\frac{1}{E_2}+2\frac{\nu_1}{E_1}\right)+\frac{1}{\sqrt{1+4\lambda^2}}\left(\frac{1}{E_1}-\frac{1}{E_2}\right)\right].\end{aligned}\right\} \tag{49}$$

Both E_i and ν_i are assumed to be represented approximately as linear functions of σ as given in Eqs. (41) and written as Eqs. (50) by using coefficients (material constants) α and β under tension and compression, respectively.

$$\left.\begin{aligned}&E_1=E_0-\alpha_1\sigma_1\,,\quad \nu_1=\nu_0-\beta_1\sigma_1\\ &E_2=E_0-\alpha_2\sigma_2\,,\quad \nu_2=\nu_0-\beta_2\sigma_2\\ &(\nu_0/E_0\approx\beta_1/\alpha_1\approx\beta_2/\alpha_2)\,.\end{aligned}\right\} \tag{50}$$

E_a and G_a can be found by substituting Eqs. (50) in Eqs. (49). If we assume $\alpha_2=0$ by taking into account that E_2 is almost invariable in compression according to experimental findings, E_a/E_0 and G_a/G_0 will reduce to

$$\left.\begin{aligned}\frac{E_a}{E_0}&=\frac{1-(1+\sqrt{1+4\lambda^2})(\alpha_1\sigma/2E_0)}{1+\dfrac{\sqrt{1+4\lambda^2}-1}{\sqrt{1+4\lambda^2}}\lambda^2\left(\dfrac{\alpha_1\sigma}{2E_0}\right)}\,,\\ \frac{G_a}{G_0}&=\frac{1-(1+\sqrt{1+4\lambda^2})(\alpha_1\tau/2E_0\lambda)}{1-\dfrac{2\lambda^2+\nu_0(1+4\lambda^2+\sqrt{1+4\lambda^2})}{\sqrt{1+4\lambda^2}(1+\nu_0)}\left(\dfrac{\alpha_1\tau}{2E_0\lambda}\right)}\,.\end{aligned}\right\} \tag{51}$$

If, as in the case of simple torsion, $\lambda\to\infty$, then G_a/G_0 can be written simply as

$$\frac{G_a}{G_0}=\frac{1-(\alpha_1\tau/E_0)}{1-(1+2\nu_0)(\alpha_1\tau/E_0)/2(1+\nu_0)}\,. \tag{52}$$

The numerical results obtained from the above with $\alpha_1/E_0=0.014$ (1/kg/mm^2) and $\nu_0=0.24$ from Fig. 25 are shown in Fig. 30 by solid lines for ratios of combined stresses. The calculated results can be seen to be in fair agreement with those of experimental results.

It is of further interest to note that a circumferential strain ε_t is produced in simple torsion. Of course, $\varepsilon_t=(\varepsilon_a)$ is absent in ductile materials in simple torsion.

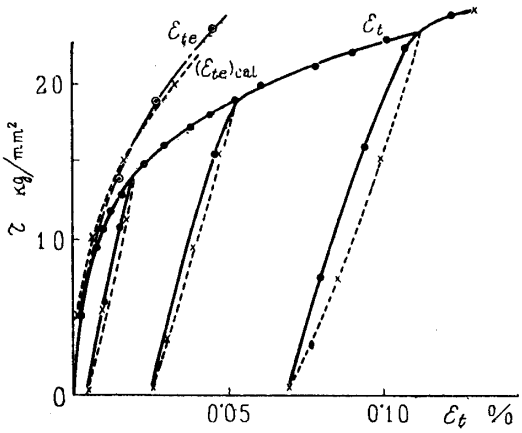

FIGURE 32. Shear stress versus circumferential strain curve under simple torsion.

However, according to Eq. (49), the elastic components of tensile strains in the axial and circumferential directions in cast irons are found by the following equation by putting $\alpha_2=0$ similarly as in the preceding.

$$\varepsilon_{te}=(\varepsilon_{ae})=\frac{1}{2\alpha_1}\frac{(\alpha_1\tau/E_0)^2}{1-(\alpha_1\tau/E_0)} \tag{53}$$

It can be seen that ε_{te} will increase more and more with an increase in τ. The curves of τ versus $\varepsilon_t(\varepsilon_{te})$ obtained in the experiments under simple torsion are shown in Fig. 32. The elastic component of the axial strain ε_{ae}, which is of the same order as ε_{te}, was also found in the same experiment by the use of a mirror extensometer. The analytical curve obtained by Eq. (53) using the same value of α_1/E_0 as in the above, is shown by the broken line in Fig. 32 which is found to coincide almost exactly with the experimental curve shown by a chain line.

3.A.3. Plastic Behavior in Deformation under Combined Tension and Torsion

When the ratio of combined stress ξ (or λ) is maintained constant during loading as in this experiment, it will be found that the axes of principal stresses will not rotate together with the principal axes of plastic strain increments, thereby simplifying the analytical treatment on plastic deformation as described in Section 1.2 (3). In the discussion on the flow behavior of ductile metals, the elastic strain components and the plastic volume change were neglected as negligible quantities. In such a case, a unique relation between the equivalent stress τ_n' and equivalent plastic strain γ_n' which are given as below after correcting the constant terms in τ_n and γ_n, was adopted with a considerable success to express the flow curve under various ratios of combined stresses.

$$\left.\begin{aligned}\tau_n'&=\sqrt{3/2}\cdot\sqrt{\sigma_{ij}'\cdot\sigma_{ij}'}=\sqrt{\sigma_1^2-\sigma_1\sigma_2+\sigma_2^2}=\sqrt{\sigma^2+3\tau^2}\,,\\ \gamma_n'&=\sqrt{2/3}\cdot\sqrt{\varepsilon_{ij}'^{p}\cdot\varepsilon'^{p}_{j}}=\sqrt{\varepsilon_{ap}^2+(\gamma_p^2/3)}\,.\end{aligned}\right\} \tag{54}$$

The law of constancy of plastic volume is disregarded by referring to this experiment on gray cast iron and γ_n' is defined in accordance with the equation.

$$\gamma_n'=(\sqrt{2}/3)\{(\varepsilon_{ap}-\varepsilon_{tp})^2+(\varepsilon_{tp}-\varepsilon_{rp})^2+(\varepsilon_{rp}-\varepsilon_{ap})^2+(3/2)\cdot\gamma_p^2\}^{\frac{1}{2}}. \tag{55}$$

The average curves of τ_n' plotted against γ_n' for each ratio of combined stresses are shown in Fig. 33 (a). It can be readily observed that little uniqueness exists between τ_n' and γ_n' for cast irons and that the equivalent stress τ_n' becomes greater as the values of ξ increase.

Next, the equivalent stress τ_n' will be further considered. The equivalent stress τ_n' is expressed in terms of the macroscopic average stress. However, due consideration must be given to the fact that large stress concentrations exist as noted previously around the edges of graphite flakes under tensile loading, which have a marked influence on the deformation behavior. Accordingly, then, a macroscopic concentrated stress $k\sigma_1$ (k=macroscopic plastic stress concentration factor) will be used by taking into account the notch effect in lieu of the tensile stress σ_1 and leaving the compressive stress σ_2 as it stands. For proximate correction, the equation for equivalent stress τ_n' in the case for biaxial stress is replaced by the following equation for notch equivalent stress $\tau_n'^*$ (Eq. 56) as heretofore introduced by Coffin [*37*].

$$\begin{aligned}\tau_n'^* &= \sqrt{(k\sigma_1)^2-(k\sigma_1)\sigma_2+\sigma_2^2} \\ &= \sigma\sqrt{\frac{k^2+1}{2}+\frac{k^2-1}{2}\sqrt{1+4\lambda^2}+\lambda^2(k^2+k+1)}\,.\end{aligned} \tag{56}$$

The value of k in the above equation denotes a macroscopic factor of stress concentration which in practice will be found to be much greater in value just at the edge of the notch. Furthermore, it is natural to expect that this value would vary with the degree of plastic deformation and decrease with an increase in the value

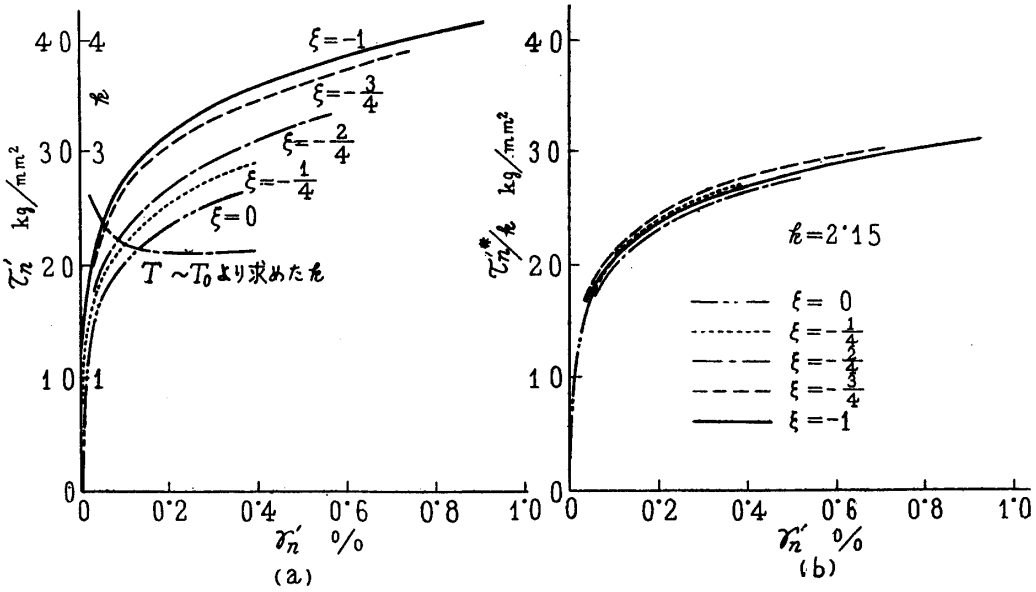

FIGURE 33. Plastic stress versus strain relationship under combined tension and torsion.

of γ'_n. However, from the plastic flow curves in Fig. 33 (b) determined with k as equal to a constant of 2.15 under various combined stresses for $\tau'_n{}^*/k$ versus γ'_n, a very satisfactory correlation curve can be found as compared with τ'_n versus γ'_n curves shown in Fig. 33 (a) in spite of the use of a specific value of k. For verification, k is estimated under the assumption that the $\tau'_n{}^*/k$ versus γ'_n curves under simple tension and torsion coincide with each other and is represented by the chain line in Fig. 33 (a). The plot reveals that k becomes smaller with an increase in γ'_n for a small deformation range i.e., $\gamma'_n<0.1$, as expected qualitatively. On the other hand, k is nearly constant after the occurrence of a certain degree of plastic deformation i.e., $\gamma'_n>0.1$. Moreover, the plastic flow curves for compression will even be found to coincide nearly with the above noted curves, if $|\sigma_c|$ is replaced by $|\sigma_c|/k$.

Although the treatment considered in the preceding is entirely empirical and approximate, it nevertheless will be found to be of practical importance in connection with the relation between τ'_n and γ'_n in ductile metals. The possibility of taking k as a constant will prove very convenient in discussing the plastic flow of cast irons in parallel with ductile metals and also in explaining the fracture stresses as will be given hereinafter.

Division B: Fracture Behavior under Combined Stresses

3.B.1. Experimental Results on Fractures under Combined Tension and Torsion

(1) *Fracture Stresses*

Plots of fracture stresses under various ratios of combined stresses are shown in Fig. 34 (a) (τ_r versus σ_r diagram) and in Fig. 34 (b) (σ_{1r} versus σ_{2r} diagram). A rough approximation seems to indicate that gray cast irons fracture principally in accordance with the "maximum principal stress law". This law, however, is not conservative and it would seem that the maximum principal tensile fracture stress would be lower with the increase in torsion as seen from the dotted line which represents the average value of fracture stresses in Fig. 34 (b). Even though the maximum shearing stress on the outer surface is taken into consideration instead of the average shearing stress along the radius, this decrease in fracture stress can be verified clearly. Although the scattering of fracture stresses is an inherent characteristic associated with cast irons, this same tendency has been found existing in tubes, for example, under internal pressure and axial compression as reported in experiments by research students [*37*] [*38*] [*39*] [*14*] and as referred to hereinafter.

The torsional strength of cast irons has been said to be greater than its tensile strength by about one and one half times as much which can be attributed to the effect of the stress gradient in a solid bar under torsion as previously explained by Professor Dr. Nakanishi [*40*]. It will be worthy to discuss this aspect in view of the evidence obtained from experiments, which disclose that the torsional

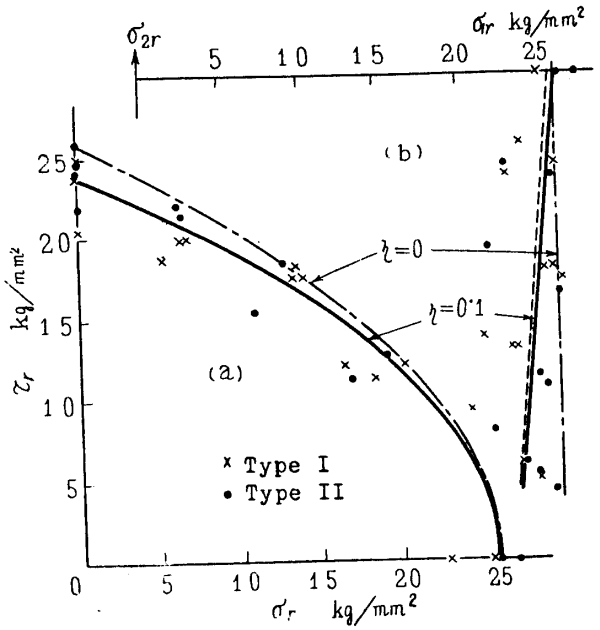

FIGURE 34. Fracture stresses under combined tension and torsion.

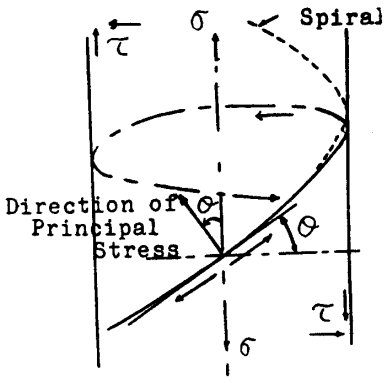

FIGURE 35. Explanation for the formation of fractured surface.

strength τ_0 of a thin walled tube is less than the tensile strength σ_0 in spite of a small stress gradient in the thin wall.

(2) *Directions of Fractured Surfaces*

A specimen subjected to simple tension fractures into two parts along a plane perpendicular to the axis, while the surface of fracture under simple torsion forms a spiral. The spiral fractured surface formed in the initial stage under combined tension and torsion progresses along the route shown by the chain line in Fig. 35 because of the change of stress distribution in the unfractured cross section thereby causing the separation into two parts. Accordingly, the direction of the

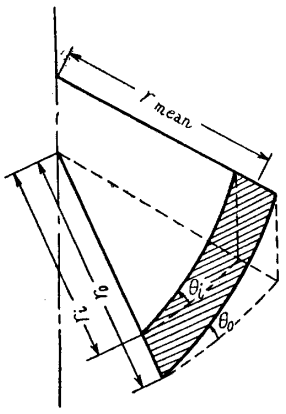

FIGURE 36. Direction of fractured surface along the thickness.

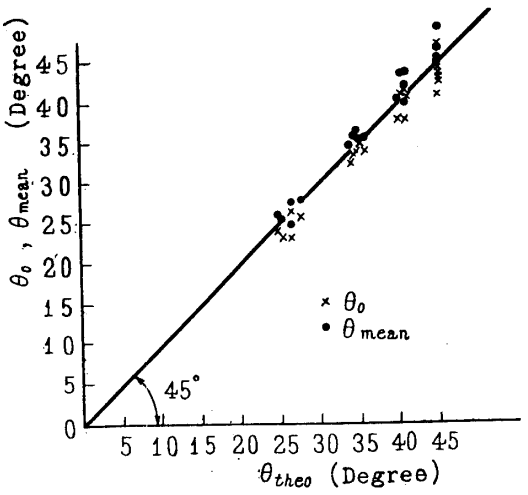

FIGURE 37. Relation between experimental derection of fractured surface (θ_0 or θ_{mean}) and theoretical one ($\theta_{\text{theo.}}$).

fractured surface on the outer surface of a specimen is measured near the point at which fracture starts. The angle thus measured is denoted by θ_0. The angle θ_{mean} at mid thickness is calculated in accordance with Eq. (57) and Fig. 36. It results from the consideration that the average shear stress is taken as the shear stress and the mean shear strain γ_{mean} at mid-thickness ($r=r_{mean}$) as the shearing strain.

$$\tan\theta_{mean}=\tan\theta_0\cdot\frac{r_0}{r_0-(t/2)} \tag{57}$$

The angle of maximum principal stress in relation to the axis of the specimen ($\theta_{theo.}$) is given by Eq. (58) in which the fracture stresses τ_r and σ_r are used.

$$\theta_{theo.}=\frac{1}{2}\tan^{-1}\left(\frac{2\tau_r}{\sigma_r}\right) \tag{58}$$

The relation between the calculated angles $\theta_{theo.}$ and the experimental angles θ_0 and θ_{mean} is plotted as shown in Fig. 37, from which it can be observed that θ_0 is slightly smaller than $\theta_{theo.}$, whereas θ_{mean} is a little greater. In any case, it can be concluded that within allowable experimental errors, the surface of fracture is formed almost normal to the direction of maximum principal stress.

(3) *Strains up to Fracture*

Table 4 shows those remarkable strain components ε_{ar} and γ_r derived from the experiments under combined stresses, in which the average values are taken from several specimens.

TABLE 4. FRACTURE STRAINS (%)

ξ	0	−1/4	−2/4	−3/4	−1
ε_{ar} (%)	0.790	0.672	0.654	0.566	0.122
γ_r (%)	0	0.713	1.102	1.665	2.269

The table reveals that the ductility increases as the magnitude of τ increases in relation to σ. Further, cast irons under compressive loading will exhibit an appreciable ductility as seen in ductile materials.

3.B.2. CONSIDERATIONS ON THE EXPERIMENTAL RESULTS DERIVED UNDER COMBINED TENSION AND TORSION

The singular behavior of deformation has been well explained with due consideration of the graphite flakes in Division A and in which, Fisher's hypothesis is recognized as reasonable. When the principal tensile stress is greater as in this combined state of stress, it will be found that the graphite flakes oriented normal to the maximum tensile stress will cause the greatest effect on fracture. Consequently, a fractured surface is formed by the linkage of a number of cavities

as seen in the microphotograph (Photo. 3) and the direction of fracture established thereby.

The fracture of gray cast irons will now be discussed with due consideration of the mechanism of fracture, applying the fracture criterion presented in Section 1.2 around the edge of such a cavity.

(1) *Explanations on the Experimental Results According to the Fracture Criterion*

The fracture studied in this experiment is one which occurs under biaxial stresses due to σ_1 (principal tensile stress) and σ_2 (principal compressive stress). On the basis of experimental evidence that σ_{1r} (principal tensile stress at fracture) is nearly constant and that the fractured surface is almost normal to σ_{1r}, we consider the most severe state of stress to exist, where the principal tensile stress acts normally to the long axis of a flat ellipsoidal cavity as shown in Fig. 38 and apply

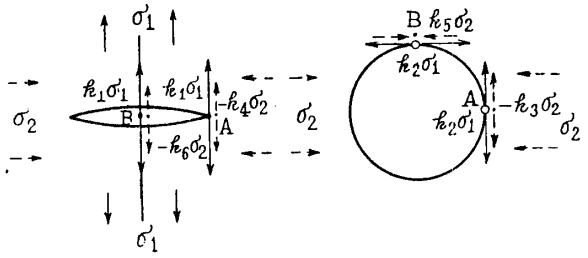

(a) side view (b) plan view

FIGUER 38. Concentrated stress state around an ellipscidal cavity under combined tension and torsion.

Eq. (2·b) in determing the tensile cleavage fracture due to a stress concentration around its tip. From Table 4, it is seen that the fracture strains are considerably small in comparison with those for ductile materials. Therefore, the strain hardening effect on fracture expressed by the third term of the right-hand side of Eq. (2·b) will be neglected which reduces to

$$\sigma_{cr}=a'+b'\Theta \tag{59}$$

The coefficient b', which expresses the weakening effect due to polyaxiality, has a negative value as noted in Section 1.2 of Part I.

The concentrated stress components around the edge of an ellipsoidal cavity under biaxial stresses σ_1 and σ_2 are shown in Fig. 38 and the elastic stress concentration factors k_i ($k_i>0$) calculated in accordance with the analysis of Sadowski etc. [*33*], are shown in Fig. 27. The stress component $k_1\sigma_1$ in the direction of σ_1, which is greatest in elasticity, will likewise be so in the plastic range, although the stress concentration will be reduced by the stress relaxation due to the plastic deformation around the edge. This deduction will be justified from the facts that the peculiarities in plastic deformation have been well explained by the use of $k\sigma_1$ instead of σ_1 because of the notch effect of graphite flakes as explained in Division A. Specific values of k_i are not definitely known; however, the local

factor will be much greater than 2, when it is considered that the macroscopic average stress concentration factor is about 2 as described in Section 3.A.3. It will be reasonable to assume that the values of k_1 correspond to $s=6\sim7$ in Fig. 27 when the decrease of notch sharpness is taken into consideration, as will be explained later. In other words, it is supposed that k_1 is about 8 to 9, k_2 and k_5 are a little greater than 1, and k_3, k_4, k_6 are small ($k_4>k_3>k_6$). Of course, the values of k_i will differ depending on the degree of plastic deformation. The most important factor k_1 will decrease with an increase of σ_1, but remains almost constant in the neighborhood of the point of fracture after plastic deformation has progressed to a certain degree as described in Section 3.A.3.

The largest stress component $k_1\sigma_1$ has a decisive effect on the fracture; however, the small stress component $-k_4\sigma_2$ or $-k_6\sigma_2$ in the same direction will contribute to the fracture, because it superposes on $k_1\sigma_1$. Furthermore, the stress components $k_2\sigma_1$, $k_5\sigma_2$ and $-k_3\sigma_2$ in the direction transverse to σ_1 will cause a secondary effect on the fracture strength through the term $b'\Theta$ in Eq. (59). Taking two typical points A and B around the edge (Fig. 38), we will compare the probability of fracture at these points. Since k_4 is greater than k_6 in the direction of σ_1, and $-k_3\sigma_2$ is tensile, while $k_5\sigma_2$ is compressive in the transverse direction, the fracture is expected to initiate at the point A whereat the fracture criterion is applied.

If the values of material constants a' and b' for a particular material and the values of k_i are known quantitatively, the fracture stresses should be determined in accordance with Eqs. (1) and (59). If the values are not known, the fracture condition can be derived by using the values of the fundamental strengths (σ_0 and τ_0 etc.). In other words, Eq. (59) is rewritten for simple tension and simple torsion respectively as follows:

$$\left.\begin{aligned} &k_1\sigma_0=a'+b'(k_1+k_2)\sigma_0/3\,,\\ &(k_1+k_4)\tau_0=a'+b'(k_1+k_2+k_3+k_4)\tau_0/3\,. \end{aligned}\right\} \tag{60}$$

Eqs. (60) can be solved with respect to a' and b' as follows:

$$\left.\begin{aligned} &a'=(k_2k_4-k_1k_3)\sigma_0\tau_0/D\,,\\ &b'=3[k_1\sigma_0-(k_1+k_4)\tau_0]/D\,,\\ &\text{where}\quad D\equiv(k_1+k_2)\sigma_0-(k_1+k_2+k_3+k_4)\tau_0\,. \end{aligned}\right\} \tag{61}$$

Substituting a' and b' thus obtained and σ_m and Θ given by the following equations

$$\left.\begin{aligned} &\sigma_m=k_1\sigma_1-k_4\sigma_2\,,\\ &\Theta=[(k_1+k_2)\sigma_1-(k_3+k_4)\sigma_2]/3 \end{aligned}\right\} \tag{62}$$

in Eq. (59) after putting σ_{cr} equal to σ_m, the fracture stresses under combined stresses can then be predicted by the following equation:

$$\sigma_1-\eta\sigma_2=\sigma_0\,,\quad \text{where}\quad \eta=(\sigma_0/\tau_0)-1 \tag{63}$$

or

$$(\tau/\tau_0)^2+(1-\eta)(\sigma/\sigma_0)+\eta(\sigma/\sigma_0)^2=1 \tag{64}$$

where k_i disappears being included in σ_0 and τ_0 of the fundamental strengths.

The line representing η equal to 0.1 is shown by the full line in Fig. 34 which shows a marked correspondence to experimental fracture stresses. Eq. (64) corresponds to the "ellipse arc theory" and Eq. (63) resembles the formulas proposed by Marin [*41*] or Sunatani [*42*]. However, the bases or concepts for derivation of these formulas are different depending on the investigators. The tensile fracture in this experiment with gray cast irons was determined with due consideration of concentration of tensile stress at the tip graphite flakes and of the state of polyaxial stress. That is, the experimental evidence that τ_0 is smaller than σ_0, can be explained by the additional tensile stress $k_4\tau_0$ due to $\sigma_2=-\tau_0$ and by the weakening of material through the superpositioning of the tensile stress in the transverse direction.

(2) *Comparison with Other Proposed Criteria*

Most proposed criteria claim the failure of materials as being determined by the shear whose critical value is expressed as a linear function of the normal stress acting on this slip plane. However, the application of such a criteria to cast irons is questionable in view of the fact that the fracture occurs in cleavage. According to the criterion proposed by Sunatani [*42*] on tensile fracture in which the critical tensile stress is expressed as a linear function of the shear stress acting on the cleavage plane, the fracture is not expected to be formed normally to the direction of maximum tensile stress. This concept has been confirmed in prefect brittle materials such as, for instance, chalk and the like, but not in cast irons under combined tension and torsion as in this experiment or under internal pressure and axial load as later described, wherein the surface of fracture was found to form almost normally to the direction of maximum tensile stress. Although the decrease in the torsional strength compared with the tensile strength can be explained in the tension—compression field according to criteria heretofore proposed, the behavior of fracture stresses relative to tension—tension field under biaxial stresses cannot be explained according to a similar viewpoint.

According to the fracture theory of Griffith [*43*] for brittle materials under biaxial stress, the fracture is assumed to occur when the highest local tensile stress around a crack reaches a fixed critical value equal to the molecular cohesion of the material. Griffith, in employing the elastic analysis of Inglis, deducted that if $3\sigma_1+\sigma_2>0$, the fracture would occur when $\sigma_1=\sigma_0$ and the fractured surface would be formed normally to the direction of σ_1. However, if the deduction is derived on the basis of an elastic analysis, the stress concentration due to σ_2 should have a contributory effect on the fracture. The author therefore cannot agree to the deduction that σ_1 is constant at fracture. If the fracture is analysed in accordance with Griffith's theory [*44*] based on the energy standpoint under simple tension, the effect due to σ_2 can be reasonably neglected as applied to perfect brittle materials with finely dispersed cracks, in view of the value of the radius of curvature at the tip of a crack, which is in the order of magnitude of atomic spacing and the decisive effect of the stress concentration due to σ_1. However, a stress relaxation takes place around the cavity of polycrystalline aggregates such as in

cast irons by plastic deformation wherefrom the polyaxial state of stress must be taken into consideration in detail in making an analysis of the fracture mechanism.

It is difficult to distinguish our concept from other proposed criteria by experimental results in such a comparatively limited field of combined stresses. However, a review of our concept will be made to show its reasonableness and justification through the application of our criteria in determining the fracture stresses under a wider field of polyaxial stresses. On this view, the experimental results under other kinds of polyaxial stresses by other research students will be cited and discussed hereafter.

3.B.3. Considerations of Fracture Results Obtained under Other Kinds of Polyaxial Stresses

(1) *Biaxial Tensile Fracture under Combined Internal Pressure and Tension*

The experiments carried out by several research students [*37*] [*38*] [*39*] [*14*] on thin-walled tubes are summarized in Fig. 39. In the case cited, the fracture under biaxial tension occurs along a plane normal to the direction of maximum tensile stress. Referring again to the tensile cleavage fracture as derived in our experiment and as described in Section 3.B.2., and the flat ellipsoidal cavity located normally to σ_1 as shown in Fig. 40 wherein $\sigma_1 > \sigma_2$, the severeness of fracture is compared at the two typical points A and B. Now, in the case where σ_2 is tensile, the fracture would be expected to initiate at the point B, whereat the fracture criterion would be applied since k_4 is greater than k_6, and $k_5\sigma_2$ is tensile, while $-k_3\sigma_2$ is compressive in the transverse direction. If the values of k_i are known, the fracture stresses under biaxial tension can be solved by using the values of a' and b' from Eq. (61) according to the same fracture mechanism as described in Section 3.B.2. However, as these values are quantitatively unknown, the following fracture condition under biaxial tension can be obtained in the same manner as in Section 3.B.2. by using the fracture stresses σ_b and σ_0 under equal biaxial tension and simple tension respectively.

$$\sigma_1+\zeta\sigma_2=\sigma_0, \quad \text{where} \quad \zeta=(\sigma_0/\sigma_b)-1 \tag{65}$$

The lines representing ζ equal to 0.1 to 0.2 are shown by the dotted lines in Fig. 39 which correspond closely with the experimental fracture stresses in the tension—tension quadrant. The fact that the principal fracture stresses under biaxial tension are smaller than σ_0 even though the tensile stress at the edge in the direction of σ_1 is reduced by a superpositioning of the compressive stress $-k_6\sigma_2$, can be explained by the extreme smallness of k_6 as well as by the major effect on the fracture by the weakening of the material strength caused by the large transverse stress component $(k_2\sigma_1+k_5\sigma_2)$. It is noteworthy that this description can be verified quantitatively by using the value of η in the tension—compression quadrant as shown by Eq. (63) and the values of k_i corresponding to s equal to 6 to 7 in Fig. 27.

(2) *Biaxial Fracture under Combined Internal (External) Pressure and Compression*

The experimental results of other investigators [37] [38] [39] on thin-walled tubes under combined internal pressure and compression are summarized in Fig. 39 and the results including the data under external pressure and compression are shown in Fig. 41. Cornet and Grassi [39] indicated that the distortion energy criterion modified by the factor of stress-concentration is consistent with the experimental data, i.e., the prediction of the fracture stress is made with the use of the constancy of the notch eqivalent stress $\tau_n'^*$ as given in Eq. (56) in stead of τ_n' and it is shown in the following equation.

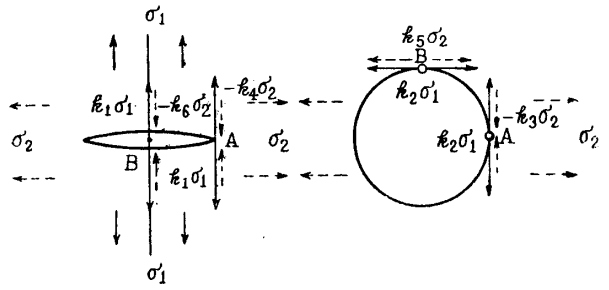

(a) side view (b) plan view

FIGURE 40. Concentrated stress state around an ellipsoidal cavity in the tension-tension field.

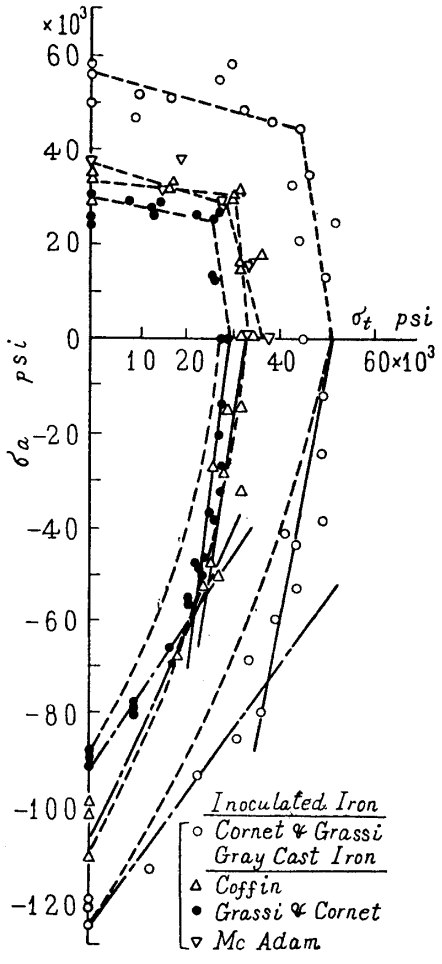

FIGURE 39. Fracture stresses on thin-walled tubes under internal pressure and axial tension (compression) by other investigators and analytical curves by the author.

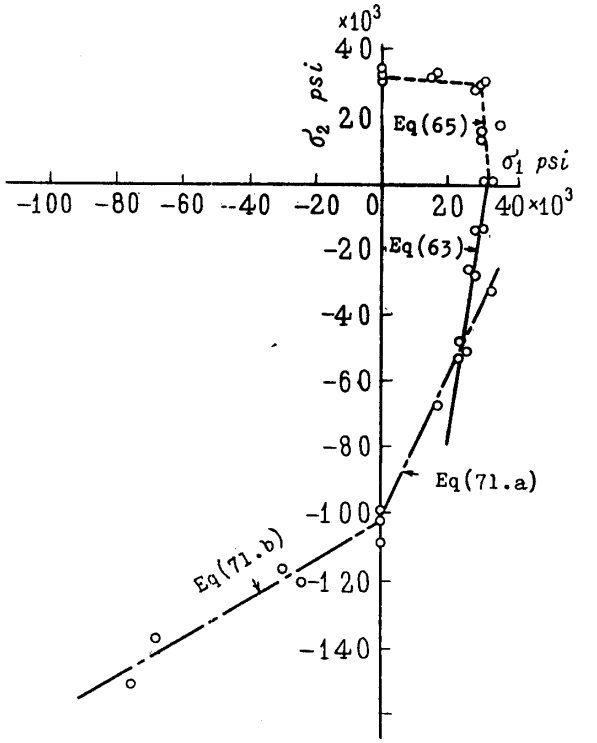

FIGURE 41. Fracture stresses on thin-walled tubes under internal (external) pressure and axial tension (compression) by Coffin [37] and analytical curves by the author.

$$(k\sigma_1)^2-(k\sigma_1)\sigma_2+\sigma_2^2=\tau_n'^{*2}=\sigma_0^2\,. \tag{66}$$

In the above equation, k denotes $|\sigma_c|/\sigma_0$, i.e., a ratio of the fracture stress in simple compression to that of simple tension. By this definition of k, the curves of these fracture stresses as shown by the dashed lines in Fig. 39 pass thru both points $-\sigma_c$ and σ_0; however, it can be seen that these curves represent conservative approximations of the experimental data for various ratios of axial to tangential stresses ranging from simple tension to simple compression. This criterion is of course emprical, wherein the fracture mechanism is disregarded and seems to be open for discussion.

The author suggested in Section 3.B.2. (1) that metals present two main types of fracture depending on the loading circumstances. As a matter of fact, the two types of fracture can be seen in this field of combined stresses, and they are discussed in accordance with the criterion given in Eqs. (2).

(i) The tensile fracture will first be considered. In the tension-compression field of stress ratios σ_2/σ_1 ranging from 0 to -3, the surface of fracture is found to form in the axial direction normal to the tangential tensile stress σ_1 due to the internal pressure, wherefrom it is made clear that the fracture is caused by the tensile fracture due to σ_1. The fracture mechanism in this case is quite similar to that under combined tension and torsion as described in Section 3.B.2. (2). The heavy lines representing η equal to 0.1 to 0.2 in Fig. 39 and Fig. 41 seem to coincide in good agreement with experimental data.

(ii) Next, the shear fracture will be considered. Under loading conditions predominantly compressive in the tension-compression quadrant, and needless to say, under simple compression or biaxial compression, the cast irons are characterized by a large ductility, obliqueness of the fractured surface and metallurgical appearance on the fractured surface similar to those in ductile metals, wherefrom the deduction is made that the fracture is caused by a shearing process. According to Griffith's theory [*43*], the fracture occurring under loading conditions, where the compression is considerably in excess of tension is basically accounted for by the mechanism of tensile fracture. Granting that this theory is reasonable as applied to fracture in perfect brittle materials such as concrete, glass etc., it is not, however, considered applicable to polycrystalline metals such as cast irons, since plastic deformation occurs at the tip of graphite flakes in cast irons and the compressive stress can be transmitted without stress raising effects as explained in Division A. Consequently, the author wonders the application of Griffith's theory to cast irons. According to Griffith's theory, the compressive strength should be eight times the tensile strength and the angle θ of the surface of fracture with the direction of σ_2 should be found to change gradually, if $3\sigma_1+\sigma_2<0$. In practice, however, the two distinguishable angles i.e., $\theta=0°$ in tensile fracture and $\theta=45°$ in shear fracture are clearly observable. Under compressive loading conditions, there exists a danger of obtaining incorrect fracture stresses; however, the experimental data given in Fig. 39 and Fig. 41 will be adopted as correct and will be discussed below.

In this case, Eq. (2·a) will be taken and applied in a manner similar to as applied to ductile metals. Since the fracture strains γ_n' up to fracture of cast irons even under simple compression are only about 10 to 15% and are considerably smaller than those of ductile metals, the third term of the right hand side of Eq. (2·a) will be neglected for a first rough approximation and the following equation will be used.

$$\tau_{cr}=a+b\Theta\,. \tag{67}$$

Since the values of material constants a and b are unknown, the fracture stresses will be represented by the two typical fracture stresses in the same manner as described before. For instance, if $-\sigma_C$ and $-\sigma_B$ are designated as the fracture stresses under simple compression and equal biaxial compression respectively, Eq. (67) can then be written as follows for these two cases.

$$\sigma_C/2=a-b(\sigma_C/3)\,,\qquad \sigma_B/2=a-b(2\sigma_B/3)\,. \tag{68}$$

Substituting a and b obtained from Eq. (68) in Eq. (67), the limiting shear fracture stress τ_{cr} can be expressed by the following equation.

$$\tau_{cr}=\{\sigma_C\sigma_B-(\sigma_B-\sigma_C)(\sigma_1+\sigma_2)\}/2(2\sigma_B-\sigma_C) \tag{69}$$

Taking into account the maximum shear stress for each of the different fields of combined stress, the conditions of fracture can be expressed by the following equations after taking τ_m equal to τ_{cr}.

$$\left.\begin{aligned}&\tau_{cr}=-\sigma_2/2\,; && 0>\sigma_1>\sigma_2\,,\\ &\tau_{cr}=-(\sigma_2-\sigma_1)/2\,; && \sigma_1>0>\sigma_2\,.\end{aligned}\right\} \tag{70}$$

From both of Eq. (69) and Eqs. (70), the fracture stresses can then be predicted from the following equations.

$$\sigma_1\{1-(\sigma_C/\sigma_B)\}-\sigma_2=\sigma_C\,;\quad 0>\sigma_1>\sigma_2 \tag{71a}$$

$$\sigma_1\{3-2(\sigma_C/\sigma_B)\}-\sigma_2=\sigma_C\,;\quad \sigma_1>0>\sigma_2 \tag{71b}$$

The theoretical curves based on Eq. (71) for the case of $\sigma_B/\sigma_C=2$ are shown by the chain lines in Fig. 39 and Fig. 41. A value of σ_B/σ_C gives a good fit with experimental results in all fields under shear fracture. It can be noted that the stress increases with an increase in the hydrostatic compression. If the effect of plastic deformation which is neglected in this case is taken into consideration, the fracture stress will not be represented by a straight line as would be given by Eq. (71) but by a curve as shown in Fig. 2 and Fig. 3 in Part I, which would seem to indicate that more accuracy can be secured.

As described above, the fracture stresses as covered in this field of study involving two types of fractures could be analytically explainable without contradicting the modes of fracture. Further, if the significance of the experiment on cast iron for the study of fracture criterion is considered as pointed out in Section 3.1, the resonableness of the author's fracture criterion seems to be established.

Conclusions

First of all, in Part I, the general phenomenological fracture criterion of polycrystalline metals was presented and the experimental fracture results with ductile metals were chiefly explained in good agreement with the analytical results. Next, in Part II, the stress and strain distributions at the moment of fracture in the minimum section of mild steel round bars having hyperbolic notches were analysed approximately and the notch brittleness phenomenon, as an example of application to practical problems, was explained by applying the fracture criterion. Lastly, in Part III, the fracture tests on thin-walled gray cast iron tubes were carried out under conditions of combined tension and torsion and it was shown that this criterion was applicable also to brittle metals. These experimental data as well as those by other research students under other kinds of combined stresses could be satisfactorily explained with due reference to the deformation mechanism in the light of the notch effect of graphite flakes.

Generally speaking, the various kinds of fracture problems could be explained to a certain extent, without contradictions to experimental evidences by holding the main two influence factors in the criterion proposed by the author. So, the reasonableness of this fracture criterion of polycrystalline metals, without distinction of the so-called ductile or brittle materials, seemed to be established. However, the author does not think that the complicating fracture problems can be fully explained by only such a criterion, in which various influence factors, e.g., the effects of stress gradients, and anisotropies etc., are neglected. To apply this criterion to various actual engineering problems, it is further desirable to know the dependence of limiting fracture stress surfaces on the temperature and the rate of stress, etc., based on the micromechanism of metals. Moreover, the quantitative data concerning the fracture stress surface is scarce. There is, therefore, a definite need for further investigation in these respects, which will be further discussed in the future after suitable preparation of the testing machines and apparatuses.

This criterion was presented for discussing the statical fracture of metals. However, we will find, even in ductile metals, that the behavior in fatigue failure is similar to that in statical fracture of brittle metals, wherefrom we can expect to discuss the fatigue failure from the same viewpoint as described herein, if we consider that the cracks formed by repeated stresses have the same effect as that of graphite flakes in gray cast iron. The author also maintains that a form of formulation of this criterion could possibly be extended for application to fatigue failure.

Acknowledgement

In closing, the author would like to express his sincere appreciation to Prof. Dr. Y. Yoshimura of the Aeronautical Research Institute, University of Tokyo for his kind advice and encouragement in connection with this work and to Mr.

Y. Takenaka, Mr. S. Abe and Mr. M. Sunagawa for their untiring assistances in carrying out the experiments.

Department of Structures
Aeronautical Research Institute
University of Tokyo, Tokyo
June 18, 1958

References

PART I:

[1] P. Ludwik; Z V D I, **71**, 44 (1927/10), 1532/1538.
[2] M. Yoshiki & T. Kanazawa; "Fune-no-Kagaku (Science of Ship)" **7**, 12 (1954)~**8**, 4 (1955).
[3] E. Orowan; Rep. on Progress in Phys. **12**. Proc. Phys. Soc. Lond. (1949), 185.
[4] C. Zener; Phys. Rev., **69** (1946), 128.
[5] J. H. Hollomon; Fracturing of Metals, Amer. Soc. Metals (1952), 262/274.
[6] N. N. Davidenkov; Dinamicheskaya ispytania Metallov, (1936), Moscow.
[7] N. F. Mott; Proc. Int. Conf. Theo. Phys. (1953), 565. Part IV. Molecules and Solids.
[8] C. Zener; Fracturing of Metals, Amer. Soc. Metals (1952), 3/31.
[9] T. Yokobori; J. Appl. Mech., **24** (1957/3), 77.
[10] D. J. McAdam; J. Appl. Mech., **8**, 4 (1941), 155/165.
[11] W. Kuntze; Mitt. dtsch. Mat-Prüf-Anst., Sonderheft **26** (1935), 133.
[12] P. W. Bridgman; Studies in Large Plastic Flow and Fracture, McGraw-Hill Co., N. Y. (1952), 26.
[13] G. Sachs; ONR Report. (1947/5).
[14] D. J. McAdam; Trans. Amer. Soc. Metals, **37** (1946), 538/566.
[15] R. Hill; Mathematical Theory of Plasticity, Oxford (1950), 300.
[16] M. Uemura; not printed, read at the meeting of the Japan Soc. Mech. Engrs. (1956/4/2).
[17] E. G. Thomson & J. E. Dorn; J. Aero. Sci., **11** (1944/4), 125/136.
[18] E. Siebel & A. Maier; Z V D I, **77**, 51 (1933/12), 1345/1349.
[19] J. H. Hollomon; Amer. Welding. Soc., **11** (1946), 534.
[20] G. Sachs; Fracturing of Metals, Amer. Soc. Metals (1952), 51.
[21] J. V. Mallendorf & J. Czochralski; Z V D I, **57** (1913), 931.
[22] J. H. Hollomon & C. Zener; Trans. Amer. Inst. Min. Metall. Engrs., Iron and Steel Division (1944), 283/297.

PART II:

[23] Y. Yoshimura & M. Uemura; Rep. of Inst. Sci. & Tech. Tokyo Univ. **6**, 3 (1952/6), 149/156.
[24] Y. Yoshimura & M. Uemura; not printed, read at the meeting of the Japan Soc. Mech. Eng. (1954/4/16).
[25] Brown etc.; Jour. Amer. Weld. Soc., **12** (1947/12), 554/559.
[26] Dana etc.; N. A. C. A. final rep. (1947/5).
[27] E. Siebel; Werkstoffansschuss, Ber. **71** (1925).
[28] P. W. Bridgman; Trans. Amer. Soc. Metals, **32** (1944), 553/574.
[29] N. N. Davidenkov & N. I. Spiridonova; Proc. A.S.T.M., **46** (1946), 1147/1158.
[30] J. Aronofsky; Jour. Appl. Mech., **18**, 1 (1951/3), 75/84.
[31] E. Orowan, J. F. Nye, W. J. Cairns; Theo. Res. Rep., No. 16/45, Am. Res. Dep., M.O.S., London (1945).

PART III:

[32] H. Udoguchi; J. Japan Soc. Mech. Engrs., **60**, 465 (1957/10), 1125/1134.
[33] M. A. Sadowski & E. Sternberg; J. App. Mech., **16**, 2 (1949/6), 149/157; **14**, 3 (1947/9), 191/201.

[*34*] E. O. Hall; J. Mech. & Phys. of Solids, **1** (1953), 227/233.
[*35*] R. E. Edwards; J. App. Mech., **18**, 1 (1951/3), 19/30.
[*36*] J. C. Fisher; G. E. Research Laboratory Rep. (1949), 7, unpublished.
[*37*] L. F. Coffin; J. App. Mech., **17**, 3 (1950/9), 233/248.
[*38*] R. C. Grassi & I. Cornet; J. App. Mech., **16**, 2 (1949/6), 178/182.
[*39*] I. Cornet & R. C. Grassi; J. App. Mech., **22**, 2 (1955/6), 172/174.
[*40*] F. Nakanishi; J. Japan Soc. Mech. Engrs., **36**, 195 (1933/7), 439/443, 444/446.
[*41*] J. Marin; McGraw-Hill Book Co., Inc. New York (1942).
[*42*] C. Sunatani; J. Japan Soc. Mech. Engrs., **25**, 74 (1922/6), 1/30.
[*43*] A. A. Griffith; First Inter. Congr. App. Mech. (Delft) (1924), 55/63.
[*44*] A. A. Griffith; Phil. Trans. Roy. Soc., **221** (1920), 163.